

Low-mass dark matter search with CDMSlite

R. Agnese,²⁴ A. J. Anderson,³ T. Aralis,¹ T. Aramaki,¹¹ I. J. Arnquist,⁸ W. Baker,¹⁷ D. Balakishiyeva,¹⁴ D. Barker,²⁶ R. Basu Thakur,^{3,25} D. A. Bauer,³ T. Binder,²⁷ M. A. Bowles,¹³ P. L. Brink,¹¹ R. Bunker,⁸ B. Cabrera,¹⁵ D. O. Caldwell,^{21,*} R. Calkins,¹⁴ C. Cartaro,¹¹ D. G. Cerdeño,^{2,18} Y. Chang,¹ H. Chagani,²⁶ Y. Chen,¹⁶ J. Cooley,¹⁴ B. Cornell,¹ P. Cushman,²⁶ M. Daal,²⁰ P. C. F. Di Stefano,⁹ T. Doughty,²⁰ L. Esteban,¹⁸ E. Fascione,⁹ E. Figueroa-Feliciano,⁷ M. Fritts,²⁶ G. Gerbier,⁹ M. Ghaith,⁹ G. L. Godfrey,¹¹ S. R. Golwala,¹ J. Hall,⁸ H. R. Harris,¹⁷ Z. Hong,⁷ E. W. Hoppe,⁸ L. Hsu,³ M. E. Huber,²² V. Iyer,⁶ D. Jardin,¹⁴ A. Jastram,¹⁷ C. Jena,⁶ M. H. Kelsey,¹¹ A. Kennedy,²⁶ A. Kubik,¹⁷ N. A. Kurinsky,¹¹ A. Leder,⁵ B. Loer,⁸ E. Lopez Asamar,² P. Lukens,³ D. MacDonell,^{19,29} R. Mahapatra,¹⁷ V. Mandic,²⁶ N. Mast,²⁶ E. H. Miller,¹³ N. Mirabolfathi,¹⁷ R. A. Moffatt,¹⁵ B. Mohanty,⁶ J. D. Morales Mendoza,¹⁷ J. Nelson,²⁶ J. L. Orrell,⁸ S. M. Oser,^{19,29} K. Page,⁹ W. A. Page,^{19,29} R. Partridge,¹¹ M. Pepin,^{26,†} M. Peñalver Martinez,² A. Phipps,²⁰ S. Poudel,²⁷ M. Pyle,²⁰ H. Qiu,¹⁴ W. Rau,⁹ P. Redl,¹⁵ A. Reisetter,²³ T. Reynolds,²⁴ A. Roberts,²⁷ A. E. Robinson,³ H. E. Rogers,²⁶ T. Saab,²⁴ B. Sadoulet,^{20,4} J. Sander,²⁷ K. Schneck,¹¹ R. W. Schnee,¹³ S. Scorza,¹² K. Senapati,⁶ B. Serfass,²⁰ D. Speller,²⁰ M. Stein,¹⁴ J. Street,¹³ H. A. Tanaka,²⁸ D. Toback,¹⁷ R. Underwood,⁹ A. N. Villano,²⁶ B. von Krosigk,^{19,29} B. Welliver,²⁴ J. S. Wilson,¹⁷ M. J. Wilson,²⁸ D. H. Wright,¹¹ S. Yellin,¹⁵ J. J. Yen,¹⁵ B. A. Young,¹⁰ X. Zhang,⁹ and X. Zhao¹⁷

(SuperCDMS Collaboration)

¹*Division of Physics, Mathematics, and Astronomy, California Institute of Technology, Pasadena, California 91125, USA*

²*Institute for Particle Physics Phenomenology, Department of Physics, Durham University, Durham DH1 3LE, United Kingdom*

³*Fermi National Accelerator Laboratory, Batavia, Illinois 60510, USA*

⁴*Lawrence Berkeley National Laboratory, Berkeley, California 94720, USA*

⁵*Department of Physics, Massachusetts Institute of Technology, Cambridge, Massachusetts 02139, USA*

⁶*School of Physical Sciences, National Institute of Science Education and Research, HBNI, Jatni 752050, India*

⁷*Department of Physics and Astronomy, Northwestern University, Evanston, Illinois 60208-3112, USA*

⁸*Pacific Northwest National Laboratory, Richland, Washington 99352, USA*

⁹*Department of Physics, Queen's University, Kingston, Ontario K7L 3N6, Canada*

¹⁰*Department of Physics, Santa Clara University, Santa Clara, California 95053, USA*

¹¹*SLAC National Accelerator Laboratory/Kavli Institute for Particle Astrophysics and Cosmology, Menlo Park, California 94025, USA*

¹²*SNOLAB, Creighton Mine #9, 1039 Regional Road 24, Sudbury, Ontario P3Y 1N2, Canada*

¹³*Department of Physics, South Dakota School of Mines and Technology, Rapid City, South Dakota 57701, USA*

¹⁴*Department of Physics, Southern Methodist University, Dallas, Texas 75275, USA*

¹⁵*Department of Physics, Stanford University, Stanford, California 94305, USA*

¹⁶*Department of Physics, Syracuse University, Syracuse, New York 13244, USA*

¹⁷*Department of Physics and Astronomy, and the Mitchell Institute for Fundamental Physics and Astronomy, Texas A&M University, College Station, Texas 77843, USA*

¹⁸*Instituto de Física Teórica UAM/CSIC, Universidad Autónoma de Madrid, 28049 Madrid, Spain*

¹⁹*Department of Physics and Astronomy, University of British Columbia, Vancouver, British Columbia V6T 1Z1, Canada*

²⁰*Department of Physics, University of California, Berkeley, California 94720, USA*

²¹*Department of Physics, University of California, Santa Barbara, California 93106, USA*

²²*Departments of Physics and Electrical Engineering, University of Colorado Denver, Denver, Colorado 80217, USA*

²³*Department of Physics, University of Evansville, Evansville, Indiana 47722, USA*

²⁴*Department of Physics, University of Florida, Gainesville, Florida 32611, USA*

²⁵*Department of Physics, University of Illinois at Urbana-Champaign, Urbana, Illinois 61801, USA*

²⁶*School of Physics and Astronomy, University of Minnesota, Minneapolis, Minnesota 55455, USA*

²⁷*Department of Physics, University of South Dakota, Vermillion, South Dakota 57069, USA*

*Deceased.

†Corresponding author.

pepi0025@umn.edu

²⁸*Department of Physics, University of Toronto, Toronto, Ontario M5S 1A7, Canada*

²⁹*TRIUMF, Vancouver, British Columbia V6T 2A3, Canada*



(Received 6 July 2017; published 17 January 2018)

The SuperCDMS experiment is designed to directly detect weakly interacting massive particles (WIMPs) that may constitute the dark matter in our Galaxy. During its operation at the Soudan Underground Laboratory, germanium detectors were run in the CDMSlite mode to gather data sets with sensitivity specifically for WIMPs with masses $<10 \text{ GeV}/c^2$. In this mode, a higher detector-bias voltage is applied to amplify the phonon signals produced by drifting charges. This paper presents studies of the experimental noise and its effect on the achievable energy threshold, which is demonstrated to be as low as $56 \text{ eV}_{\text{ee}}$ (electron equivalent energy). The detector-biasing configuration is described in detail, with analysis corrections for voltage variations to the level of a few percent. Detailed studies of the electric-field geometry, and the resulting successful development of a fiducial parameter, eliminate poorly measured events, yielding an energy resolution ranging from $\sim 9 \text{ eV}_{\text{ee}}$ at 0 keV to $101 \text{ eV}_{\text{ee}}$ at $\sim 10 \text{ keV}_{\text{ee}}$. New results are derived for astrophysical uncertainties relevant to the WIMP-search limits, specifically examining how they are affected by variations in the most probable WIMP velocity and the Galactic escape velocity. These variations become more important for WIMP masses below $10 \text{ GeV}/c^2$. Finally, new limits on spin-dependent low-mass WIMP-nucleon interactions are derived, with new parameter space excluded for WIMP masses $\lesssim 3 \text{ GeV}/c^2$.

DOI: 10.1103/PhysRevD.97.022002

I. INTRODUCTION

In the last few decades, astronomical observations have consistently indicated that most of the matter content of the Universe is nonluminous and nonbaryonic dark matter [1,2]. There is strong evidence that dark matter is distributed in large halos encompassing the visible matter in galaxies, including the Milky Way. If this dark matter is composed of particles that interact with normal matter through a nongravitational force, it may be possible to directly detect it in laboratory experiments.

The first generation of direct detection experiments searched for dark matter in the form of weakly interacting massive particles (WIMPs), with particle masses spanning from a few GeV/c^2 to a few TeV/c^2 , and interaction strengths with normal matter less than the weak force [3,4]. These searches were partly motivated by supersymmetric theories in which the lightest neutral particles are WIMPs and thus natural dark matter candidates. However, no confirmed WIMP signals have been found, and there is no evidence as yet for supersymmetry at the LHC [5,6].

Other theoretical models have been developed, motivated by possible symmetries between normal and dark matter (e.g., asymmetric dark matter [7]) or the possibility of a parallel dark sector that may contain many dark matter particles [8]. These new models predict dark matter particles with masses $<10 \text{ GeV}/c^2$, stimulating experiments to search in this region.

WIMPs are expected to scatter elastically and coherently from atomic nuclei, producing nuclear recoils (NRs). Neutrons also produce nuclear recoils but often scatter multiple times in a detector; WIMPs interact too weakly to scatter more than once. Residual radioactivity in the experimental apparatus predominantly interacts with atomic electrons, causing electron recoils (ERs) that are the

dominant source of background. Experiments try to reduce the rate of all backgrounds using layers of radiopure shielding and through the detection of multiple types of signals to discriminate between electron and nuclear recoils.

The nuclear-recoil energy spectrum expected from simple WIMP models is featureless and quasiexponential [3,9]. The differential nuclear-recoil rate is

$$\frac{dR}{dE_r} = \frac{N_T m_T}{2m_\chi \mu_T^2} [\sigma_0^{\text{SI}} F_{\text{SI}}^2(E_r) + \sigma_0^{\text{SD}} F_{\text{SD}}^2(E_r)] \mathcal{I}_{\text{halo}}, \quad (1)$$

where m_χ and m_T are the masses of the WIMP and the target nucleus, respectively, $\mu_T = m_\chi m_T / (m_\chi + m_T)$ is the reduced mass of the WIMP-target system, N_T is the number of nuclei per target mass, and E_r is the energy of the recoiling nucleus. The spin-independent (SI) and spin-dependent (SD) cross sections for the WIMP-nucleus scattering are each factored into a total zero-energy cross section $\sigma_0^{\text{SI/SD}}$ and nuclear form factor $F_{\text{SI/SD}}^2(E_r)$.

The rate's dependence on the astrophysical description of the WIMP halo is encompassed by the halo-model factor $\mathcal{I}_{\text{halo}}$. This factor depends on the velocities of the WIMPs in the halo's frame \mathbf{v} and the velocity of the Earth with respect to the halo \mathbf{v}_E as

$$\mathcal{I}_{\text{halo}} = \frac{\rho_0}{k} \int_{v_{\min}}^{v_{\max}} \frac{f(\mathbf{v}, \mathbf{v}_E)}{v} d^3 v, \quad (2)$$

where ρ_0 is the local dark matter mass density, k is a normalization constant, and the halo's velocity distribution with respect to the Earth $f(\mathbf{v}, \mathbf{v}_E)$ is integrated from the minimum v_{\min} to the maximum v_{\max} WIMP velocities that can cause a recoil of energy E_r . The maximum velocity is related to the Galactic escape velocity v_{esc} , while the minimum velocity is $v_{\min} = \sqrt{m_T E_r / 2\mu_T^2}$. Assuming the

standard Maxwellian velocity distribution with a characteristic velocity v_0 (see Sec. VII A) gives an expression for $\mathcal{I}_{\text{halo}}$ as [10]

$$\mathcal{I}_{\text{halo}} = \frac{k_0}{k} \frac{\rho_0}{2yv_0} \begin{cases} \text{erf}(x+y) - \text{erf}(x-y) - \frac{4}{\sqrt{\pi}}ye^{-z^2} & 0 < x < z-y \\ \text{erf}(z) - \text{erf}(x-y) - \frac{2}{\sqrt{\pi}}(y+z-x)e^{-z^2} & z-y < x < y+z \\ 0 & y+z < x, \end{cases} \quad (3)$$

where $x = v_{\min}/v_0$, $y = v_E/v_0$, $z = v_{\text{esc}}/v_0$, $k_0 = (\pi v_0^2)^{3/2}$, and $k = k_0[\text{erf}(z) - (2/\sqrt{\pi})z \exp(-z^2)]$. The final case in this expression is set to zero to avoid unphysical negative rates.

Figure 1 shows the predicted differential rates on a germanium target for three low-mass WIMPs with spin-independent WIMP-nucleon cross sections of 10^{-41} cm^2 . Lowering the experimental energy threshold boosts the signal-to-background ratio, assuming a flat background spectrum, and reduces the dependence of the WIMP signal on astrophysical uncertainties. A lower threshold thus dramatically increases an experiment's sensitivity to lower-mass WIMPs.

The Cryogenic Dark Matter Search low ionization threshold experiment (CDMSlite) uses a technique developed by the SuperCDMS Collaboration to reduce the experiment's energy threshold and increase sensitivity to low-mass WIMPs [11,12]. This paper presents further details of the published CDMSlite analyses and some new results. The organization of the paper is as follows. Section II discusses the experimental technique, CDMSlite data sets, and data-reduction improvements. Section III discusses the analysis

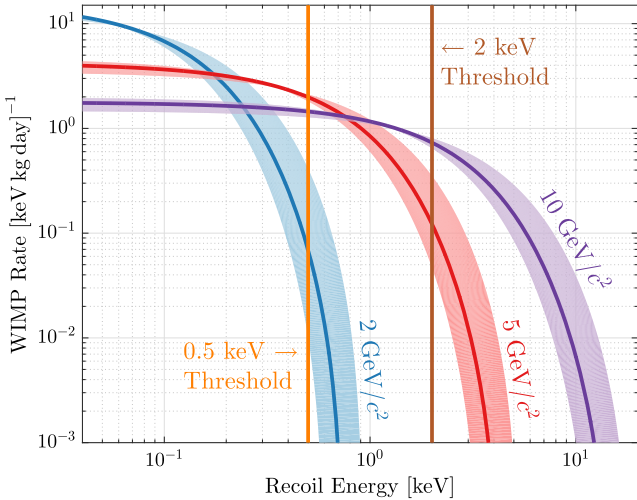


FIG. 1. Differential rates for WIMP recoils on a germanium target as functions of recoil energy. WIMPs with a WIMP-nucleon spin-independent cross section of 10^{-41} cm^2 and masses of 2, 5, and $10 \text{ GeV}/c^2$ are considered. The bands encompassing each curve are computed by varying the astrophysical parameters of the dark matter halo within known observational uncertainties. The vertical lines designate example nuclear-recoil thresholds of 0.5 and 2 keV, respectively.

and removal of noise. Section IV discusses an energy resolution model and energy thresholds. Section V discusses the effects of bias instability in the analyses and the steps taken to account for those effects. Section VI discusses the definition of a fiducial volume and its effect on backgrounds. Finally, new WIMP results are given in Sec. VII based on the effects of astrophysical uncertainties on the spin-independent WIMP-nucleon scattering limit presented in Ref. [12] and new spin-dependent WIMP-nucleon scattering limits.

II. DESCRIPTION OF THE EXPERIMENT

The SuperCDMS Soudan experiment was located at the Soudan Underground Laboratory and used the same cryogenics system, shielding, and electronics as the earlier CDMS II experiment [13,14]. Five towers, each consisting of three germanium interleaved Z-sensitive ionization and phonon detectors (iZIPs), were operated from 2011 to 2015 [15]. Each iZIP was roughly cylindrical with a ~ 76 mm diameter, ~ 25 mm height, and ~ 600 g mass. Particle interactions in these semiconductor crystals excite electron-hole charge pairs as well as lattice vibrations (phonons). The top and bottom circular faces of an iZIP are instrumented with electrodes for sensing the charge signal and tungsten transition edge sensors (TESs) for measuring phonons. The electrons and holes are drifted to the electrodes by applying a bias voltage across the crystal (nominally 4 V), while athermal phonons are absorbed by Al fins that are coupled to the TESs. During data taking, the output traces from the detectors were recorded (“triggering” the experiment) if the analog sum of any detector's raw phonon traces exceeded a user-set hardware threshold [16].

Measuring both the charge and phonon signals allows for discrimination between NRs and ERs through the ionization yield Y ,

$$Y(E_r) \equiv \frac{E_Q}{E_r}, \quad (4)$$

where E_Q is the charge signal and, for electron recoils, $E_Q \equiv E_r$. The efficiency of producing electron-hole pairs is lower for nuclear recoils, leading to yields of $Y \sim 0.3$ for $E_r \gtrsim 10$ keV. Below this energy, electronic noise causes the widths of the ER and NR populations to increase until they largely overlap at ~ 1 keV, and complex background modeling must be used to separate the recoil types [17]. This, coupled with the additional difficulty of separating

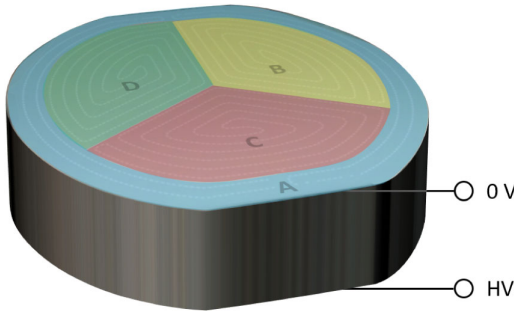


FIG. 2. Schematic showing the general coverage of the four phonon read-out channels (A–D) overlaying the sensor pattern for the CDMSlite detector. The sensors on the bottom side are exclusively used for applying the high-voltage bias (HV) and are not read out. All sensors on the top side are held at ground.

low-energy events from noise, requires the typical iZIP analysis threshold to be set above the overlap region.

A. CDMSlite

In 2012, SuperCDMS began running detectors in the alternate CDMSlite operating mode, where the detector potential difference was raised to 50–80 V. The standard iZIP electronics and biasing configuration were adapted for this higher-voltage operating mode; phonon and ionization sensors on one side of the detector were set to the given bias, while all of the sensors on the opposite face were held near ground potential. Figure 2 shows the phonon sensor layout and biasing scheme of the CDMSlite detectors. The sensors on the grounded side of the detector were then read out. The limitations of the CDMS II electronics board prohibited two-sided operation as the board could not simultaneously be floated to a potential and read out.

The CDMSlite operating mode takes advantage of phonon amplification via the Neganov-Trofimov-Luke (NTL) effect [18,19]. Electrons and holes liberated by the initial recoil drift across the detector, driven by the applied electric potential.¹ During transport, they collide with Ge atoms and reach a scattering-limited drift velocity of $\mathcal{O}(10^6 \text{ cm s}^{-1})$ in $\lesssim 1 \text{ ns}$. When the kinetic energy of the charge carriers is $\gtrsim 30 \text{ meV}$, high rates of optical and intervalley phonon scattering limit further acceleration and cause them to reach a terminal velocity. The additional work done in drifting these charge carriers, as they collide with the lattice (50–80 eV per electron-hole pair at the biases under discussion), is emitted as phonons. The residual kinetic energy of $\sim 30 \text{ meV}$ per electron-hole pair, along with the band gap energy of 0.74 eV [21], is eventually released as phonons, called relaxation or recombination phonons, when the charge carriers relax to the Fermi sea near detector

¹This discussion of electron and hole transportation in a germanium crystal is taken from the rigorous calculations in Ref. [20]. See, e.g., Chaps. 2 and 4 of the reference for further details.

boundaries. The phonons emitted during charge transport are called NTL phonons, and the net energy in these phonons, E_{NTL} , is the work done by the electric field

$$E_{\text{NTL}} = N_{e/h} e \Delta V. \quad (5)$$

Here, $N_{e/h}$ is the number of electron-hole pairs created in the recoil, e is the elementary charge, and ΔV is the potential difference traversed by the pairs. ΔV is nominally the absolute value of the bias applied by the power supply V_b . The advantage of operating at relatively high bias potentials is an amplification of the charge signal (as observed in the phonon signal) due to increased NTL-phonon production.

The total phonon energy in the crystal is thus the sum of ionization-associated NTL phonons, primary phonons created at the initial recoil site, and relaxation phonons created near detector surfaces. The sum of the primary and relaxation phonons is E_r , and thus the total energy is

$$E_t = E_r + E_{\text{NTL}} = E_r + N_{e/h} e \Delta V. \quad (6)$$

The number of electron-hole pairs created by a recoil depends on the recoil type. For electron recoils in germanium, the average (photoexcitation) energy required to generate a single electron-hole pair is taken to be $\varepsilon_\gamma = 3 \text{ eV}$ [22]. This gives $N_{e/h} = E_Q / \varepsilon_\gamma = Y(E_r) E_r / \varepsilon_\gamma$, where Eq. (4) is used for the second equality. Substituting this last expression into Eq. (6) gives

$$E_t = E_r \left(1 + Y(E_r) \frac{e \Delta V}{\varepsilon_\gamma} \right). \quad (7)$$

As only one of two faces of an iZIP are read out in CDMSlite mode, the energy absorbed by the operable phonon sensors is half that of Eq. (7).

The calibration of the measured phonon signal proceeds in three steps, with three corresponding energy scales, using Eq. (7) assuming $\Delta V = V_b$. The first step is to convert the raw output to the “total phonon energy scale,” with units of keV_t, using calibration data taken at the standard operating bias of 4 V and the expectation from Eq. (7) (see Sec. V A). Converting the calibrated E_t to the interaction’s E_r requires knowledge of the yield. Because CDMSlite only measures phonons, the yield cannot be constructed on an event-by-event basis, and a model for $Y(E_r)$ is required. Two further energy scales are defined corresponding to the assumed ER/NR recoil type. The ER scale is stretched considerably compared to the NR scale with its smaller electron-hole production efficiency; this further increases the signal-to-background ratio for CDMSlite.

The recoil energies are next calibrated assuming all events are ERs, i.e., $Y(E_r) = 1$, called “electron-equivalent” energy in units of keV_{ee} and denoted by $E_{r,ee}$. This scale is useful for characterization of the backgrounds, which are primarily ERs. An ER calibration is available

from electron-capture decays of ^{71}Ge . Thermal neutron capture on ^{70}Ge (20.6% natural abundance) creates ^{71}Ge , which then decays by electron-capture with a half-life of 11.43 days [23]. The K -, L -, and M -shell binding energies of the resulting ^{71}Ga are 10.37, 1.30, and 0.16 keV, respectively [24]. In the experiment, ^{71}Ge was created in the detector by exposing it to a ^{252}Cf source two to five times per CDMSlite data set. The K -shell peak, clearly visible in the data following such an activation, is used to calibrate the energy scale to keV_{ee} and to correct for any changes in the energy scale with time (see Sec. V).

WIMP scatters are expected to be NRs; so a nuclear-recoil energy is ultimately constructed, called “nuclear-recoil equivalent” energy in units of keV_{nr} and denoted by $E_{\text{r,nr}}$. The calibration to keV_{nr} is performed by comparing Eq. (7), assuming the detector sees the full V_b bias, for an ER and NR with the same E_t , and solving for $E_{\text{r,nr}}$,

$$E_{\text{r,nr}} = E_{\text{r,ee}} \left(\frac{1 + eV_b/\epsilon_\gamma}{1 + Y(E_{\text{r,nr}})eV_b/\epsilon_\gamma} \right), \quad (8)$$

where $Y(E_{\text{r,nr}})$ is the yield as a function of nuclear-recoil energy, for which a model is needed. The model used is that of Lindhard [25],

$$Y(E_{\text{r,nr}}) = \frac{k \cdot g(\epsilon)}{1 + k \cdot g(\epsilon)}, \quad (9)$$

where $g(\epsilon) = 3\epsilon^{0.15} + 0.7\epsilon^{0.6} + \epsilon$, $\epsilon = 11.5E_{\text{r,nr}}(\text{keV}_{\text{nr}})Z^{-7/3}$, and Z is the atomic number of the material. For germanium, $k = 0.157$. The Lindhard model has been shown to roughly agree with measurements in germanium down to $\sim 250 \text{ eV}_{\text{nr}}$ [26,27], although measurements in this energy range are difficult, and relatively few exist [28–30]. The SuperCDMS Collaboration has a campaign planned to directly measure the nuclear-recoil energy scale for germanium (and silicon) down to very low energies, since this will be required for the upcoming SuperCDMS SNOLAB experiment.

B. Data sets and previous results

A single detector was operated in CDMSlite mode during two operational periods, Run 1 in 2012 and Run 2 in 2014.² The initial analyses of these data sets, published in Refs. [11,12], respectively, applied various selection criteria (cuts) to the data sets and used the remaining events to compute upper limits on the SI WIMP-nucleon interaction. These limits were computed using the optimum interval method [31], the nuclear form factor of Helm [9,32], and assuming that the SI interaction is isoscalar. Under this last assumption, the WIMP-nucleon cross section σ_N^{SI} is related

²Only a single detector was operated for each run due to limitations of the Soudan electronics and to preserve the live time for the standard iZIP data taken concurrently.

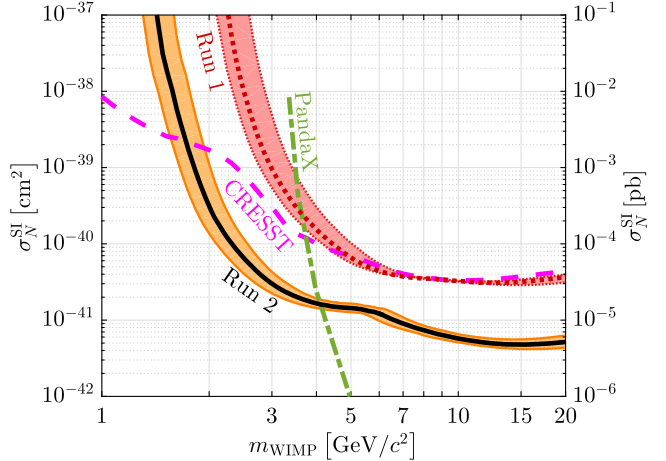


FIG. 3. Spin-independent WIMP-nucleon cross section 90% upper limits from CDMSlite Run 1 (red dotted curve with red uncertainty band) [11] and Run 2 (black solid curve with orange uncertainty band) [12] compared to the other (more recent) most sensitive results in this mass region: CRESST-II (magenta dashed curve) [33], which is more sensitive than CDMSlite Run 2 for $m_{\text{WIMP}} \lesssim 1.7 \text{ GeV}/c^2$, and PandaX-II (green dot-dashed curve) [34], which is more sensitive than CDMSlite Run 2 for $m_{\text{WIMP}} \gtrsim 4 \text{ GeV}/c^2$. The Run 1 uncertainty band gives the conservative bounding values due to the systematic uncertainty in the nuclear-recoil energy scale. The Run 2 band additionally accounts for the uncertainty on the analysis efficiency and gives the 95% uncertainty on the limit.

to σ_0^{SI} in Eq. (1) as $\sigma_0^{\text{SI}} = (A\mu_T/\mu_N)^2 \sigma_N^{\text{SI}}$, where μ_N is the reduced mass of the WIMP-nucleon system.

CDMSlite Run 1 was a proof of principle and the first time WIMP-search data were taken in CDMSlite mode. For Run 1, the detector was operated at a nominal bias of -69 V , and an analysis threshold of $170 \text{ eV}_{\text{ee}}$ was achieved. In an exposure of just 6.25 kg d (9.56 kg d raw), the experiment reached the SI sensitivity shown in Fig. 3 (labeled “Run 1”), which was world leading for WIMPs lighter than $6 \text{ GeV}/c^2$ at the time of publication [11].

The total efficiency and spectrum from Run 1 are shown in Figs. 4 and 5, respectively. In addition to the ^{71}Ge -activation peaks, the K -shell activation peak from ^{65}Zn is visible in the Run 1 spectrum at $8.89 \text{ keV}_{\text{ee}}$ [24]. The ^{65}Zn was created by cosmic-ray interactions, with production ceasing once the detector was brought underground in 2011, and decayed with a half-life of $\tau_{1/2} \approx 244\text{d}$ [35]. The analysis threshold was set at $170 \text{ eV}_{\text{ee}}$ to maximize dark matter sensitivity while avoiding noise at low energies (see Sec. III C). To compute upper limits, the conversion from keV_{ee} to keV_{nr} was performed using the standard Lindhard-model k value [Eq. (9)] of 0.157. Limits were also computed using $k = 0.1$ and 0.2, chosen to represent the spread of experimental measurements [26–30], to bound the systematic due to the energy-scale conversion. As shown in Fig. 3, this uncertainty has a large effect at the lowest WIMP masses.

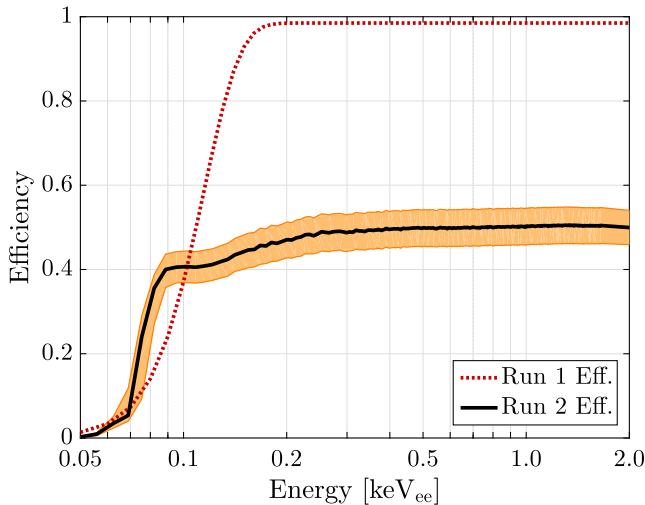


FIG. 4. Total combined trigger and analysis efficiencies for Run 1 (red dotted curve) and Run 2 (black solid curve with orange 68% uncertainty band). The implementation of a fiducial-volume cut is primarily responsible for the reduction in efficiency at high recoil energies between the two analyses.

In Run 2, the detector was operated with a bias of -70 V, the analysis threshold was further reduced because of improved noise rejection, and a novel fiducial-volume criterion was introduced to reduce backgrounds. The total efficiency and spectrum from this run are compared to those of the first run in Figs. 4 and 5. Because of the lower analysis threshold, decreased background, and a larger exposure of 70.10 kg d (80.25 kg d raw), the experiment

yielded even better sensitivity to the SI interaction than Run 1 [12], as shown in Fig. 3 (labeled “Run 2”). The second run was split into two distinct data periods (see Sec. III C), labeled “Period 1” and “Period 2,” that had analysis thresholds of 75 and 56 eV_{ee}, respectively.

For the Run 2 result, the uncertainties of the analysis were propagated into the final limit by simulating 1000 pseudoexperiments and setting a limit with each. The median and the central 95% interval from the resulting distribution of limits, at each WIMP mass, are taken as the final result given in Fig. 3. For each pseudoexperiment, the keV_{ee} energy of the events and thresholds were constant. The analysis efficiencies, as indicated by the band in Fig. 4, were sampled, as was the Lindhard-model k within a range of $0.1 \leq k \leq 0.2$. The uncertainty in the energy conversion dominates the band in Fig. 3, with the next-largest uncertainty being that of the fiducial-volume acceptance efficiency (Sec. VI B).

C. Pulse fitting and energy measurement

Several improvements were made in the analysis of Run 2 data, compared to that of the Run 1 data, by the introduction of a new data-reduction algorithm used to extract energy and position information about scatters in the detector. To motivate and understand this new algorithm, the dynamics of phonon detection and the older algorithms, which are still used for many parts of the analyses, are first discussed.

The phonon sensors cover only $\sim 5\%$ of the surfaces of iZIP detectors. Phonons have a $\sim 40\%$ probability of absorption when they strike an aluminum sensor fin³ but are reflected when striking an uninstrumented surface. The phonons continue to rebound between surfaces of the crystal until they are absorbed by, or become lost to, the sensors [36]. Phonons become undetectable by the sensors either by falling below the aluminum superconducting gap energy or by being absorbed through nonsensor materials (e.g., stabilizing clamps). The small fraction of phonons striking a fin at the first surface interaction produces an early absorption signal that is concentrated close to the location of the interaction, while the majority of the phonons contribute to a later absorption signal that is mostly homogeneous throughout the detector. The phonon pulse shape thus contains both position and energy information about the initial scatter in the earlier and later portions of the signal trace, respectively.

The CDMSlite analyses employ three algorithms based on optimal filter theory (see Appendix B of Ref. [37]) to extract the position and energy information of the underlying event based on the measured pulse shapes and

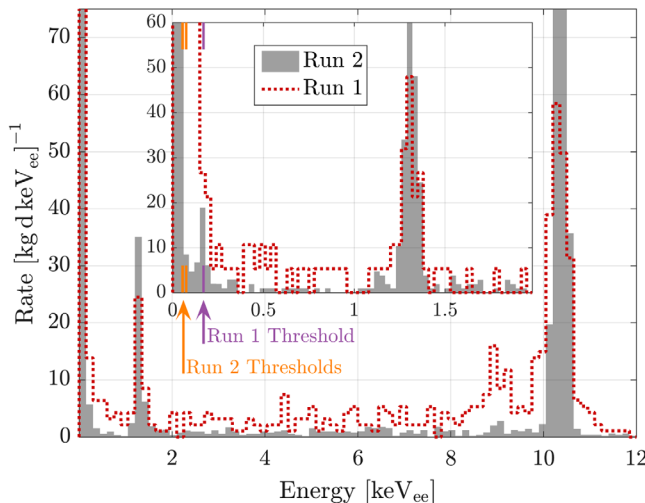


FIG. 5. Measured efficiency-corrected spectra for Run 1 (red dotted curve) and Run 2 (gray shaded area). The ^{71}Ge -activation peaks at 10.37 and 1.30 keV_{ee} are prominent in both spectra, and the peak at 0.16 keV_{ee} is additionally visible in the Run 2 spectrum. The ^{65}Zn K-shell electron-capture peak is also visible at 8.89 keV_{ee} in the Run 1 spectrum. *Inset:* an enlargement of the spectra below 2 keV_{ee} with bins five times smaller and the runs’ analysis thresholds given by the extended and labeled tick marks.

³This value of 40% is determined by tuning a phonon simulation in a detector to match recorded pulses. Specifically, how quickly pulses return to their baseline values is sensitive to this absorption probability.

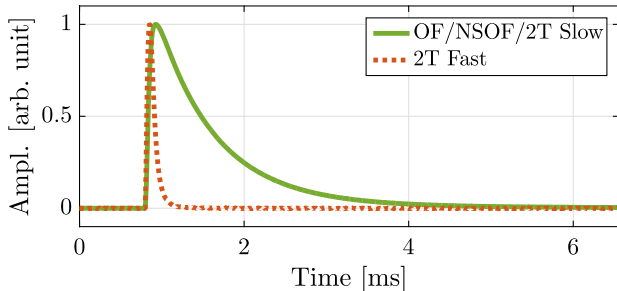


FIG. 6. Templates used for the standard OF, NSOF, and 2T-fit algorithms for CDMSlite analysis. The green solid curve is the single trace used for the OF, NSOF, and 2T-fit slow templates, which is derived from averaging high-energy traces. In the 2T fit, the slow template’s amplitude carries the main energy information. The 2T-fit fast template (orange dotted), is derived by considering the differences between the slow template and the traces used in the slow template’s derivation. In the 2T fit, the fast template’s amplitude captures the position information from the signal trace. The maxima of the amplitudes (Ampl.) are scaled to unity in the figure.

amplitudes. For these algorithms, the signal trace $S(t)$ is generally modeled as a template, or linear combination of templates, $A(t - t_0)$, which can be shifted by some time delay t_0 , and Gaussian noise $n(t)$ as

$$S(t) = aA(t - t_0) + n(t), \quad (10)$$

where the template is scaled by some amplitude a . The optimal values of a and t_0 are then found by minimizing, in frequency space, the χ^2 between the left- and right-hand sides of Eq. (10). The amplitude, time delay, and goodness-of-fit χ^2 value are returned by the algorithms.

The first algorithm is called the “standard” optimal filter (OF). The OF algorithm fits a single template to a trace, as in Eq. (10), without attempting to account for the position dependence in the early portion of the trace. The template was created by averaging a large number of high-energy traces taken from the ^{71}Ge K -shell capture peak and can be seen in Fig. 6. The energy estimate from this fit, the amplitude a in Eq. (10), has poor resolution because of the position dependence. The position of an event’s initial scatter in the detector can be estimated by fitting the traces from each individual channel of a given event and comparing the fit amplitudes among the channels: channels of which the sensors are nearer to the interaction will have a larger amplitude than those of which the sensors are farther away.

The second algorithm is called the “nonstationary” optimal filter (NSOF) (see Appendix E of Ref. [38]), and it produces an energy estimator that is less affected by the early-trace position dependence. The NSOF uses the same single template as in the OF fit but treats the residual deviations between the trace and the template as nonstationary noise. This procedure deweights the parts of the trace that show larger variance and results in a more

accurate energy estimator. Additionally, the NSOF fit is calculated only for the summed trace of each individual detector, which also serves to reduce, but does not completely eliminate, the effect of position dependence on the energy estimate. The NSOF is not useful for computing position information about the initial scatter.

The third algorithm, utilized for the first time with CDMSlite Run 2 data, is called the “two-template” optimal filter (2T fit) (see Appendix E of Ref. [38] and Chap. 10 of Ref. [39]). The 2T fit uses a linear combination of two different templates, replacing $aA(t - t_0)$ with $\sum_{i=s,f} a_i A_i(t - t_0)$. The two templates are shown in Fig. 6 and are labeled the “slow” and “fast” templates. The slow template is the same template used in the OF and NSOF fits. The fast template is derived by considering the differences between the slow template and the traces used to define it, termed the residual traces. To calculate this template, the residuals with negative amplitude are inverted before all residuals are averaged. The inversion conserves the shape and is needed because the average of the residuals without the inversion is zero by definition. The 2T fit returns an energy estimator—the amplitude of the slow template—which, like the NSOF, is less affected by the position of the initial scatter than the OF fit, but it also returns the amplitude of the fast template which encodes position information. The 2T fit is applied to each individual channel’s trace as well as the summed trace. An example of this fit is shown in Fig. 7. Negative fast-template amplitudes are expected in fit results and indicate greater distance from the initial scatter.

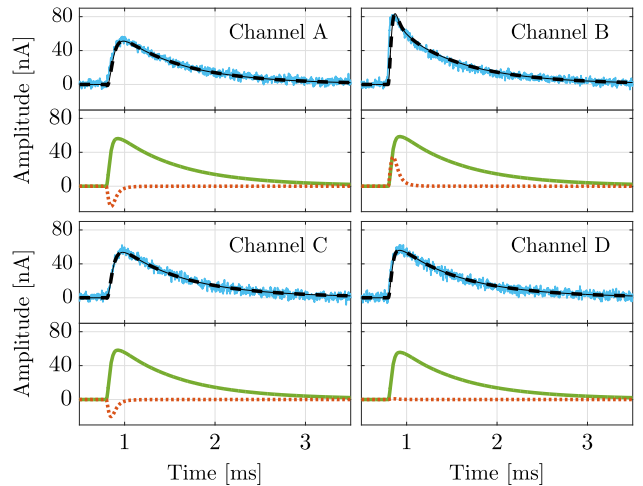


FIG. 7. Results of the 2T-fit algorithm for an example event chosen from the ^{71}Ge L -shell capture peak in Run 2. The traces and fits from all four phonon channels, labeled A–D (where channel A is the outer ring) are given. For each channel, the raw trace (blue solid) is compared to the final total fit (black dashed) which is a linear combination of the slow (green solid) and fast (orange dotted) templates. The channel with the largest fast-template amplitude, channel B for this event, is the channel of which the sensors are closest to the initial recoil.

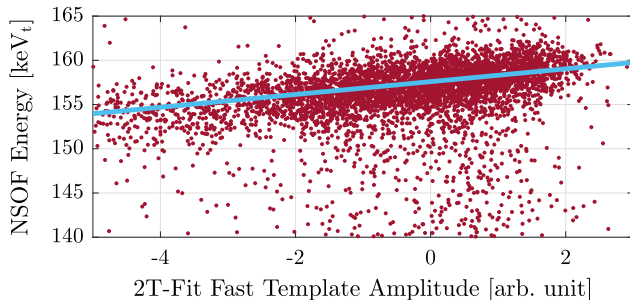


FIG. 8. NSOF-fit energy estimator as a function of the 2T-fit fast-template amplitude from the summed trace. The high-density band of events is the ${}^{71}\text{Ge}$ K -shell activation line. Residual position dependence is reflected in the slope of the band. This dependence is corrected according to the straight-line fit shown by the solid line. The location of the peak at $\sim 155 \text{ keV}_t$ is discussed in Sec. V A.

In the Run 1 analysis, the energy estimator from the NSOF algorithm was used without any further corrections for position dependence. For the Run 2 analysis, the NSOF energy estimator was again used, but an additional position correction was applied based on the 2T fit information. As shown in Fig. 8, a correlation between the fitted NSOF energy estimate and 2T-fit fast-template amplitude is observed. The linear fit to this correlation is used for the correction.⁴ In the Run 2 analysis, a cut was placed to remove events for which the NSOF fit returned large χ^2 values to ensure that the energy estimator was reliable. Such a cut removes events that have more than one pulse in the trace, or that exhibit a distorted pulse shape due to TES saturation. The signal efficiency for the cut is near 100% as computed via a pulse simulation that is described in Sec. III C 2. No poorly fit events were observed above threshold in the smaller Run 1 WIMP-search data set, and thus such a cut was unnecessary.

III. STUDY AND REMOVAL OF NOISE

Understanding the noise in the readout wave forms is crucial for optimizing the low-energy analysis and achieving the desired low-energy thresholds using the CDMSlite technique. Studies from both runs showed that the noise depended on both bias voltage and time. Most crucially, cryocooler-induced low-frequency noise was present and limited the Run 1 threshold. A combination of timing correlations with the cryocooler and pulse-shape fitting was used in Run 2 to reject this background.

⁴The energy estimator extracted from the slow-template amplitude of the 2T fit has more position dependence than that of the NSOF, manifesting itself in a stronger correlation with the 2T-fit fast-template amplitude. After correcting for this correlation, the performance is very similar with a marginally better resolution of the NSOF-based algorithm in the ${}^{71}\text{Ge}$ K -shell peak.

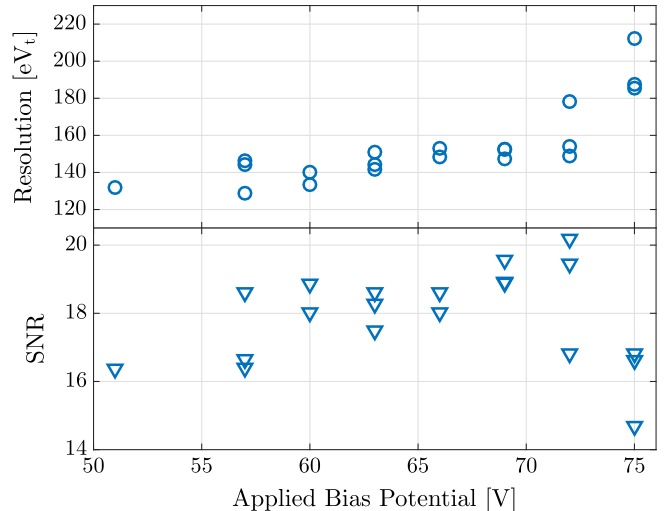


FIG. 9. Baseline resolution (top) and the corresponding SNR (bottom) as a function of the applied bias potential. Each point represents a single 3 h long data set taken prior to Run 2. The resolution and SNR increase and decrease, respectively, past ~ 70 V in applied bias. The average uncertainty for each point is 3.6 eV_t for the resolution and 0.39 for the SNR. The additional variation seen at a given bias is likely a result of time dependence of the noise. For reference, $1 \text{ keV}_t \approx 66 \text{ eV}_{ee}$.

A. Dependence of noise on bias potential

The operating potential difference for each run was determined by studying the noise as a function of the applied potential difference. The baseline resolution as a function of this potential difference is shown in Fig. 9 for data taken prior to Run 2. The resolution slowly increased until the potential difference passed ~ 70 V, where a larger increase was observed. Taking the potential difference up to 85 V resulted in greatly increased noise signaling the start of detector breakdown. A recoil-energy-independent signal-to-noise ratio (SNR) was also considered by comparing the measured signal and noise to the $V_b = 0$ V case. The signal, according to Eq. (7) (assuming a yield of unity), was then $1 + eV_b/\varepsilon_\gamma$. The noise was the measured resolution in Fig. 9 divided by an assumed zero-volt resolution of 120 eV_t. The SNR is also shown in Fig. 9, with a peak SNR at ~ 70 V. These studies were used to determine the operating potential differences of 69 and 70 V for the two runs, respectively.

B. Time dependence of noise

For iZIP detectors, the charge collection efficiency deteriorated after being biased and operated for longer than ~ 3 h. This decrease in collection efficiency was caused by charges becoming trapped on impurity sites in the crystal instead of drifting fully to the electrodes [40]. To avoid the collection efficiency loss, data were taken in 3 h long periods called “series.” At the end of each series, the detectors were grounded and exposed to photons from light

emitting diodes. These photons created excess electron-hole pairs that neutralized the impurity sites. This light exposure increased the temperature of the detectors, and a 10 min cool-down period was required before beginning the next series. In detectors operated in CDMSlite mode, trapped charges resulted in excess noise, and steps were developed to minimize this effect.

During Run 1 operation, the noise in the CDMSlite detector was seen to be excessively high immediately after the detector was biased to its fixed operating point at the start of a series. The noise decayed quasiexponentially with time, presumably due to the tunneling of trapped charges, until an asymptotic level was achieved (see Appendix B of Ref. [38]). Noise-trace data from a typical series are shown in Fig. 10, where the reconstructed energy has higher rms earlier in the series. The excess noise amplitude decayed with an exponential time constant $\tau \sim 10$ min. In Run 1, the data taken during the first 4τ following the application of the bias voltage were discarded, as a balance between

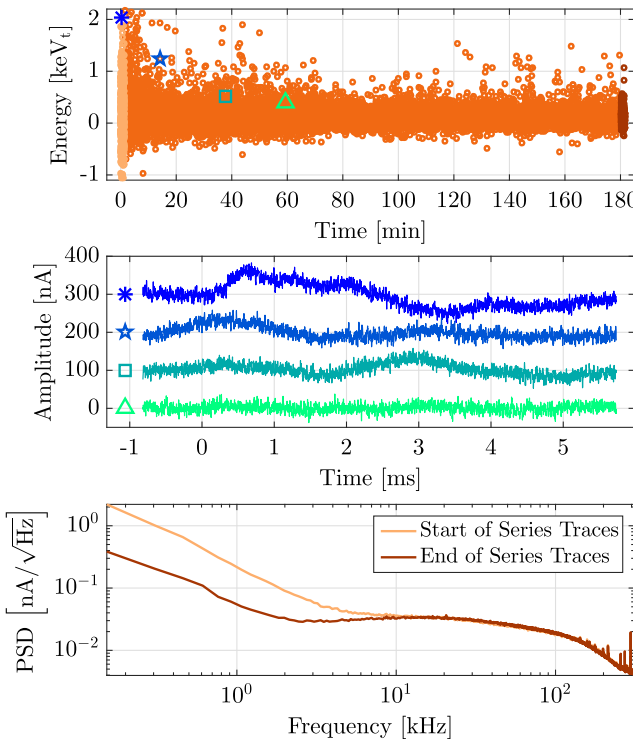


FIG. 10. *Top:* total phonon energy, or noise, as a function of time since biasing in Run 1. The noise decays quasiexponentially with time; four example events are given by noncircular markers. The first and last 500 traces are highlighted in light and dark orange, respectively. The noise distribution is offset from 0 keV_t as the energy-estimating algorithm tends to fit to upward noise fluctuations. For reference, 1 keV_t \approx 66 eV_{ee}. *Middle:* raw traces of the events marked in the top panel. Traces are shifted by 100 nA with respect to each other for clarity. *Bottom:* power spectral densities (PSDs) for the noise at the start (light orange) and end (dark orange) of the series. The earlier traces have more power below \sim 10 kHz.

live time and optimal baseline resolution. Thus, in Run 1, only \sim 70% of the data collected could be used for the analysis.

In Run 2, the high initial noise was avoided by holding the detector at a larger potential difference than the operating voltage prior to the start of each series, after which the bias was dropped to the operating voltage. Under the assumption that the initial noise is due to the release of trapped charges, this initial bias at higher potential difference allows for all traps accessible at the lower potential difference to be cleared. This operational procedure is termed “prebiasing,” and the SuperCDMS data acquisition system (DAQ) was configured to prebias before each data series in Run 2. The prebiasing procedure was as follows:

- (i) At the end of each series, ground the detector while it is exposed to the photons from the light emitting diodes.
- (ii) During the necessary 10 min cool-down period, hold the detector at a potential difference of -80 V.
- (iii) After the cooldown, lower the potential difference to the -70 V operating voltage, and begin data taking for the next series.

The effectiveness of prebiasing can be seen in Fig. 11, which compares the baseline noise distributions for series which were, or were not, prebiased. The series were taken during the bias scan prior to Run 2, described in Sec. III A, and were thus taken at various biases (the data in Fig. 9 were prebiased). The widths of the distributions which were

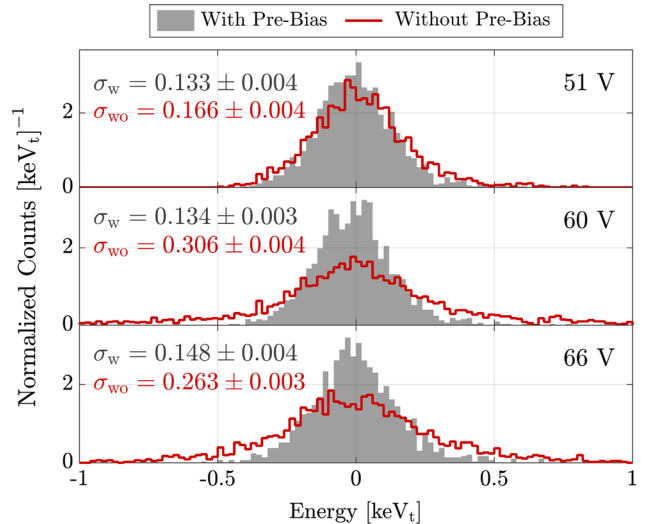


FIG. 11. Baseline noise distribution for series that were prebiased (gray area) and series that were not prebiased (red curve) taken at potential differences of 51/60/66 V (top/middle/bottom). The Gaussian-equivalent widths (see Sec. IV A) of the distributions with σ_w and without σ_{wo} prebiasing are also given, in keV_t. The thinner distribution widths for prebiased series compared to nonprebiased series demonstrates the effect of prebiasing. For reference, 1 keV_t \approx 66 eV_{ee}.

prebiased are smaller than those which were not, as shown by the values in the figure.

C. Low-frequency noise

In Run 1, the baseline noise resolution was 14 eV_{ee}, and the detector had 50% trigger efficiency at 108 eV_{ee}. The analysis threshold was set at 170 eV_{ee} to avoid being overwhelmed by a source of \sim kHz noise (labeled “low frequency”) that dominated the triggered-event rate below \sim 200 eV_{ee}. The primary source of this low-frequency noise was identified as vibrations from the Gifford-McMahon cryocooler used to intercept heat traveling down the electronics stem via the readout cables. The cryocooler cycled at \sim 1.2 Hz but stimulated higher-frequency vibrations that produced phonons in the detectors, including the CDMSlite detector, that were observable as low-frequency signals in the read-out traces. The low-frequency noise was also present in Run 2, as shown in the top panel of Fig. 12. The electronic noise distribution is centered at 0 keV_t, and the low-frequency noise distribution is dominant from

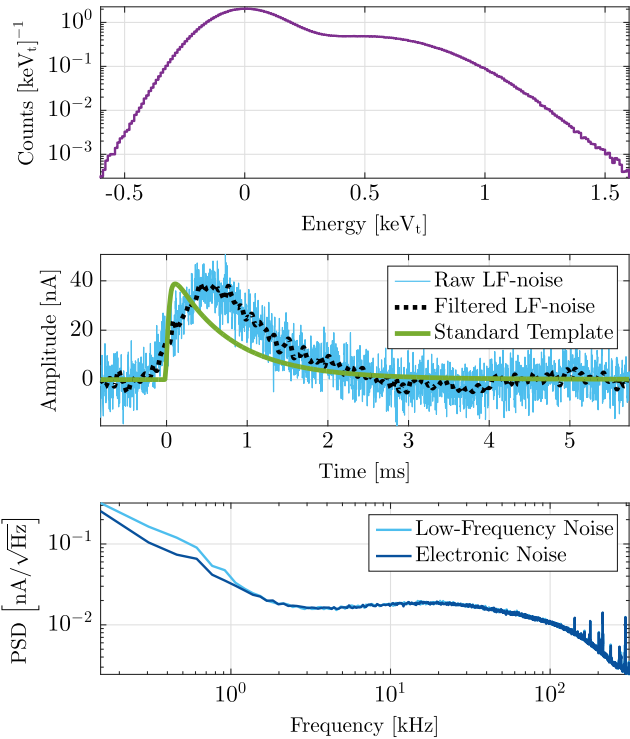


FIG. 12. *Top:* Run 2 noise distribution. The electronic-noise distribution is centered at \sim 0 keV_t while the low-frequency noise distribution dominates from 0.5–1.5 keV_t. For reference, 1 keV_t \approx 66 eV_{ee}. *Middle:* raw (thin light blue solid) and filtered (thick black dotted) trace from a typical low-frequency noise event compared to the standard-event template (thick green solid), derived from high-energy ^{71}Ge K-shell events. The difference in pulse shape is most evident between 0 and 2 ms. *Bottom:* power spectral densities (PSDs) for 500 low-frequency (light blue) and electronic (dark blue) noise traces. The low-frequency noise population has more power below \sim 1 kHz.

0.5–1.5 keV_t. These events were identified as noise by studying their pulse shape compared to the OF algorithm template as shown in the middle panel of Fig. 12. In comparing the noise power spectral densities from 500 events (each) of low-frequency and electronic noise (bottom panel of Fig. 12), the low-frequency noise events have more power below \sim 1 kHz.

The push to reject low-frequency noise, and subsequently reach a lower analysis threshold, for Run 2 occurred in two steps. The first step was to characterize the low-frequency noise with regard to the timing of the cryocooler and identify blocks of calendar time that had similar low-frequency noise behavior (Sec. III C 1). The second step was to define a rejection criterion based on the pulse shape of individual events and to tune the position of the rejection threshold individually between the different calendar blocks (Sec. III C 2).

1. Cryocooler timing characterization

For Run 2, two accelerometers were placed on and near the cryocooler to monitor vibrations. Custom processing electronics were also installed to record the cryocooler cycle in the DAQ [38,39]. Comparing the time stamps of recorded events to those of the cryocooler gives, for each event, the time since the start of the previous cryocooler cycle \hat{t}_- . The precision of \hat{t}_- is 3 ms and is dictated by the precision of the accelerometer read-out. The cryocooler cycle (\sim 830 ms) starts with a compression event, which causes the largest amount of vibrational noise, and includes an expansion phase, \sim 400 ms after the compression, which also causes noise. These two parts of the cryocooler cycle are distinctly observed in Fig. 13, which histograms the

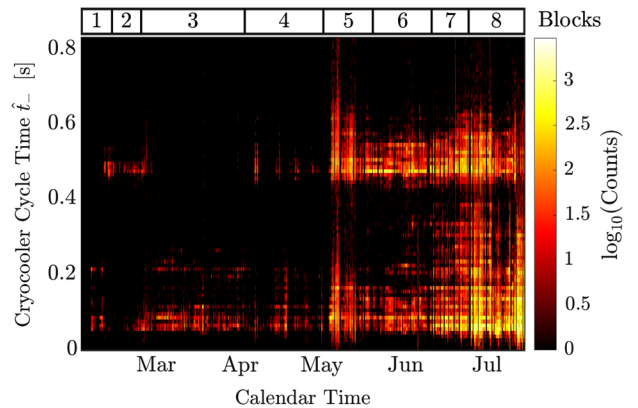


FIG. 13. Number of low-energy triggered events for Run 2 Period 1 in the two-dimensional plane of cryocooler time, \hat{t}_- , and calendar time in 2014. The color scale is logarithmic with empty bins mapped to black. The rate of low-frequency noise injection evolved throughout the run because of the deterioration of the cryocooler, ranging from 0 to >1000 counts per bin. The boundaries of the eight time blocks defined after applying a smoothing filter to the histogram are given in the bar labeled “Blocks” above the plot.

number of low-energy triggered events (dominated by low-frequency noise) in both \hat{t}_- and calendar time.

During the course of Run 2, the cryocooler degraded further, and the rate of events triggered by low-frequency noise greatly increased. The rate increase was accompanied by a change in the low-frequency noise induction pattern as seen on the right side of Fig. 13. During this part of the run, low-frequency noise appeared throughout the entirety of the cryocooler cycle. This obvious deterioration demanded a room-temperature warm-up of the experiment for servicing of the cryocooler cold head and divided the run into the aforementioned Periods 1 and 2.

The low-frequency noise induction was characterized by developing and applying a smoothing filter to the histogram in Fig. 13 [39]. As the average number of particle interactions expected in each bin is $\mathcal{O}(10^{-3})$, bins with $10^2\text{--}10^3$ counts are clear outliers due to low-frequency noise. Correlations between neighboring bins are also indicators of low-frequency noise, as the noise typically occurs in bursts in calendar time and cryocooler time. Applying a smoothing filter then deemphasizes true noise fluctuations, high-count bins surrounded by low-count bins, and allows better identification of times with a high low-frequency noise rate. Using the filtered data, eight blocks in calendar time were defined such that the low-frequency noise behavior within each block was roughly consistent. These time blocks are indicated at the top of Fig. 13.

In Period 2 of Run 2, the accelerometers were not configured in the DAQ. This oversight was not discovered until after the end of the run, and thus the cryocooler timing information was not available in Period 2. Instead, four time blocks were defined in Period 2 based on shifts in the energy scale and general noise environment. The first two blocks occurred during the end of September and the beginning of October. The energy scale noticeably shifted between these periods (see Sec. V C and Fig. 21). The last two blocks, taken at the end of October and beginning of November, each contained a small amount of live time and coincided with a number of unrelated calibration and noise studies. Small shifts in the noise environment were observed between these blocks. In total, Run 2 was divided into 12 nonoverlapping time blocks.

2. Pulse-shape discrimination

The criterion that was ultimately used to remove low-frequency noise from the data set was based on pulse shape, tailored to the different time blocks. A new trace template was created by averaging a large number of low-frequency noise events; these traces were identified as those which triggered the detector, were in the energy range characteristic of low-frequency noise, and took longer than 1 ms to reach their maximum value. This template is compared to the standard OF template in Fig. 14. This new template was then fit to every trace using the single-template OF

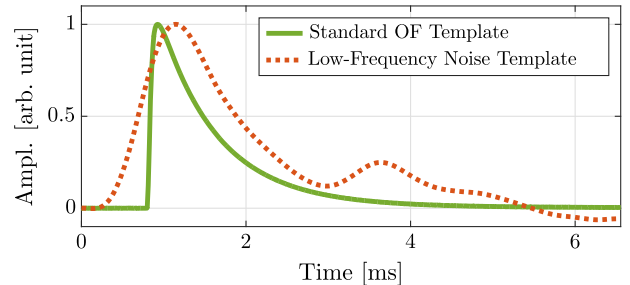


FIG. 14. Template traces for the standard OF (green solid) and low-frequency noise (orange dotted) fits. The templates were generated by averaging many events' pulse shapes, which removed uncorrelated noise. Details of the low-frequency noise template generation are discussed in the text, and the standard OF template definition is discussed in Sec. II C. The maxima of the amplitudes (Ampl.) are scaled to unity in the figure.

algorithm described in Sec. II C [i.e., using the new template for $A(t)$ in Eq. (10)], returning a goodness-of-fit parameter χ_{LF}^2 . A discrimination parameter $\Delta\chi_{\text{LF}}^2$ was then defined as

$$\Delta\chi_{\text{LF}}^2 \equiv \chi_{\text{OF}}^2 - \chi_{\text{LF}}^2, \quad (11)$$

where χ_{OF}^2 is the goodness-of-fit parameter from the single-template OF algorithm using the standard template.

Example planes of $\Delta\chi_{\text{LF}}^2$ versus energy are given in Fig. 15 for time blocks 2 and 7, both from Period 1. Pulse shapes that better fit the standard OF template have negative $\Delta\chi_{\text{LF}}^2$ and lie on a downward opening parabola, while those which better fit the low-frequency noise shape have positive $\Delta\chi_{\text{LF}}^2$. The cut was tuned piecewise with three components. The first is a flat portion tuned to reject the worst (based on $\Delta\chi_{\text{LF}}^2$) $\sim 10\%$ of the electronic noise distribution. The second component was tuned on the good-event parabola, where the mean μ and width σ of the $\Delta\chi_{\text{LF}}^2$ distribution in a number of energy bins extending to 400 keV_t were computed and the threshold fit to the $\mu + 5\sigma$ points from each bin. The $\mu + \sigma$ values were used to ensure a loose cut at high energies where no low-frequency noise was expected. However, in order for the threshold to be tight enough to exclude the low-frequency noise distribution at low energies, an additional constraint of an upper bound on the y-intercept was also required. The third component was based on a two-dimensional kernel-density estimate [41] of the $\Delta\chi_{\text{LF}}^2$ and energy of low-energy triggers (dominated by the low-frequency noise). The threshold was taken as a convex hull around the largest $n\sigma$ contour from the estimate, where n varied from 2.5–5 in steps of 0.5. The tuning of this position was set individually for each time block based on a manual scan of borderline traces; i.e., if any trace that appeared to be contaminated by low-frequency noise was found, n was increased. Thus, the cut was tighter in time blocks of greater low-frequency noise rate and looser in time blocks with a lower low-frequency noise rate. The time blocks shown in Fig. 15

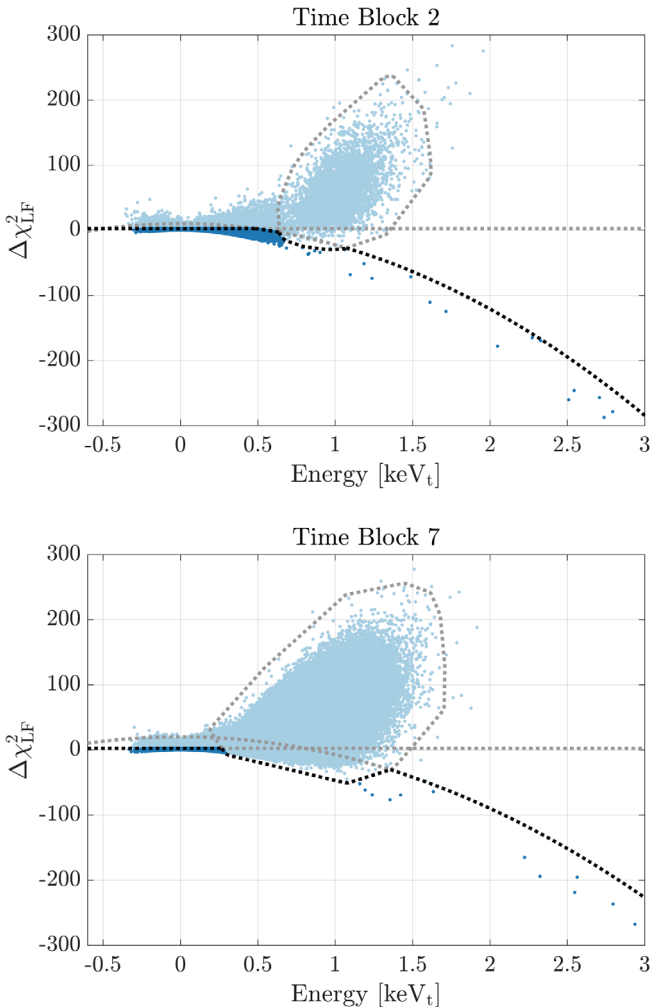


FIG. 15. $\Delta\chi^2_{\text{LF}}$ as a function of total phonon energy for time blocks 2 (top) and 7 (bottom) showing the three portions of the low-frequency noise rejection cut (dotted) with the defining portion at any given energy darkened. Low-frequency noise events cluster near $\sim 1 \text{ keV}_t$, while good events fall on a downward opening parabola. The major difference between the two subplots is the difference in low-frequency noise: time block 2 shows low noise, while time block 7 is more noisy. Events above any portion of the cut are rejected (light blue), while those below are retained (dark blue). Time block 2 is relatively less noisy, while time block 7 is relatively more noisy. The contour portion in block 2 cuts more loosely (2.5σ) than in block 7 (5σ) because of the changing low-frequency noise environment throughout the run. A preselection cut removing events with unusually high NSOF χ^2 values has been applied in these figures and, for reference, $1 \text{ keV}_t \approx 66 \text{ eV}_{\text{ee}}$.

represent examples of low and high cryocooler-induced triggered noise rates, with looser and tighter cut thresholds, respectively.

The joint efficiency of three pulse-shape-based cuts, including the low-frequency noise cut, was determined by generating simulated traces, applying the same pulse-fitting techniques as the experimental data, and computing the

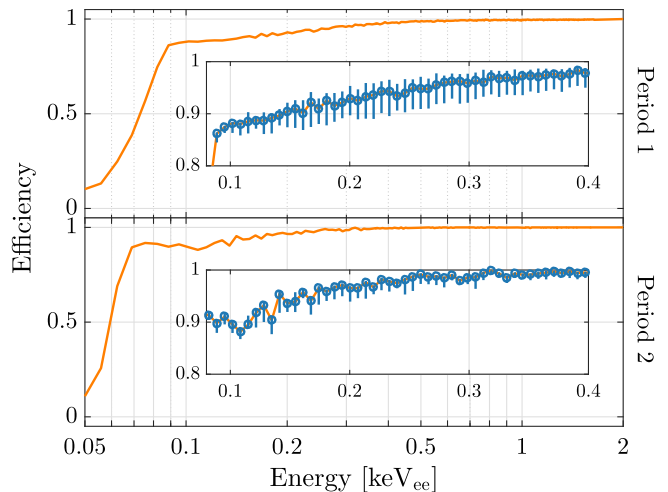


FIG. 16. Efficiency of the pulse-shape based cuts for Run 2 Period 1 (top) and Period 2 (bottom) as a function of electron-equivalent energy. Almost all loss in efficiency is due to the low-frequency noise cut, with the sharp drop in efficiency below $100 \text{ eV}_{\text{ee}}$ due to the kernel-density-estimate portion of that cut. The insets give an enlargement in the $\mathcal{O}(100 \text{ eV}_{\text{ee}})$ range, where the systematic uncertainty from varying the pulse shape, shown by the error bars, is largest. The average statistical uncertainty for each bin, due to the number of traces simulated, is 1.2%.

fraction of simulated events that pass the cuts as a function of energy. Efficiency was also assessed for cuts that remove events with high NSOF-returned χ^2 values and electronic-glitch events, which are events with pulses that have uncharacteristically fast fall times. The simulated traces were constructed by combining a measured noise trace, selected from those recorded routinely throughout the WIMP search, and a noiseless template scaled to a desired amplitude. The procedure was repeated using three templates of different shapes to assess the systematic uncertainty of the efficiency due to pulse shape. The templates were the standard OF-fit template and two new templates defined as $T_{\pm} = T_s \pm \alpha T_f$, where $T_{s/f}$ are the slow and fast templates from the 2T fit (Fig. 6). α was chosen to be 0.125 to encompass the observed fast-to-slow template ratio of events in the ^{71}Ge K-shell peak. The efficiency of these cuts is shown in Fig. 16, including the uncertainty from varying the template shape. The loss in efficiency due to the non-low-frequency noise cuts is $< 5\%$ at any given energy bin. The large decrease below $100 \text{ eV}_{\text{ee}}$ is where the kernel-density-estimate portions of the low-frequency noise cut are active. The sharp onset of this decrease differs by time block, while the more gradual decrease seen in the figure (particularly for Period 1) is due to averaging over all time blocks. Also note that, while the cut thresholds, such as those shown in Fig. 15, are defined in the keV_t energy scale, the efficiency must be evaluated in the energy scale used in the final analysis, keV_{ee} .

IV. RUN 2 ENERGY RESOLUTION AND THRESHOLD

The low-frequency noise cut described in the previous section allowed the event selection in Run 2 to avoid events resulting from known noise sources. The remaining noise distribution was studied to measure the baseline resolution of the detector, which in turn was used to model the detector's energy resolution. The analysis threshold, however, was constrained by the detector's efficiency for triggering on low-energy events, i.e., the trigger threshold.

A. Run 2 energy resolution model

The total energy resolution $\sigma_T(E_{r,ee})$ for the detector was modeled as

$$\sigma_T(E_{r,ee}) = \sqrt{\sigma_E^2 + \sigma_F^2(E_{r,ee}) + \sigma_{PD}^2(E_{r,ee})} \quad (12)$$

$$= \sqrt{\sigma_E^2 + BE_{r,ee} + (AE_{r,ee})^2}, \quad (13)$$

where σ_E is the baseline resolution caused by electronic noise, $\sigma_F(E_{r,ee})$ describes the additional width due to electron-hole pair statistics including the Fano factor [42], and $\sigma_{PD}(E_{r,ee})$ is the broadening due to position dependence. The electronic noise is energy independent. The variance due to electron-hole pair statistics can be written as $FE_\gamma E_{r,ee} \equiv BE_{r,ee}$, where F is the Fano factor. Previous measurements at higher temperatures give $F = 0.13$ [43], and using $\epsilon_\gamma \approx 3$ eV [22] per electron-hole pair gives an expectation of $B = 0.39$ eV_{ee}. Finally, variations due to position dependence are expected to be proportional to energy; this final term may also include other effects that scale with energy.

The baseline resolution can be measured using the reconstructed energy of noise-only events taken throughout the run. When applied to noise traces, the algorithms described in Sec. II C tend to fit to the largest noise fluctuation, which biases the fit toward nonzero amplitudes. This is undesirable for characterizing the baseline noise distribution; for this study, the time delay is forced to be zero, and the corresponding energy distribution for Run 2 is shown in Fig. 17. To avoid efficiency effects, no cut against low-frequency noise was applied, and thus the distribution is slightly skewed to positive energy. A simple Gaussian fit would not be representative of the distribution; the resolution is determined via a Gaussian-equivalent computation: the 1σ -equivalent is taken as one-half the energy between the 15.87th and 84.13th percentiles (the $\mu \pm \sigma$ values for a normal distribution). Repeating the procedure for a variety of histogram bin sizes gives an estimate of the uncertainty. The baseline resolution determined in this way is 9.25 ± 0.11 eV_{ee}.

The resolution model of Eq. (13) with parameters σ_E , B , and A was fit to the peaks, weighted by their uncertainties,

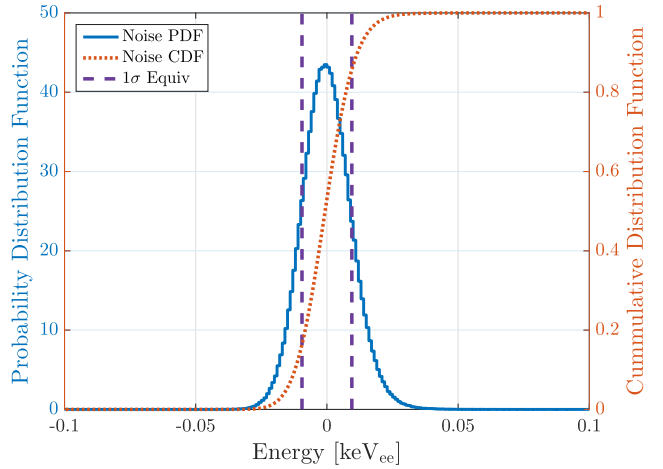


FIG. 17. Reconstructed energy probability distribution function (PDF) of noise-only events in Run 2 (blue solid, left vertical axis) with the corresponding cumulative distribution function (CDF) (orange dotted, right vertical axis). The 1σ -equivalent is taken as half the distance between the 15.87th and 84.13th percentiles (dark purple dashed) and is 9.26 ± 0.11 eV_{ee}.

at four different energies: the zero-energy baseline distribution and the three ^{71}Ge -activation peaks at 10.37 keV_{ee} (K shell), 1.30 keV_{ee} (L shell), and 0.16 keV_{ee} (M shell). The resolution of each of these peaks is given in Table I. The final fit is given in Fig. 18 with a goodness-of-fit per degree of freedom $\chi^2/\text{dof} = 1.22$. Because of the small uncertainty on the baseline resolution, and the weighting of the fit, $\sigma_E = 9.26 \pm 0.11$ eV_{ee} is very similar to the measured value. The best-fit Fano coefficient is $B = 0.64 \pm 0.11$ eV_{ee}, while the position-dependence coefficient is $A = (5.68 \pm 0.94) \times 10^{-3}$. The last two parameters are strongly anticorrelated with a Pearson's product-moment correlation coefficient of $\rho_{AB} = -0.984$. Repeating the fit with B fixed to the expected value gives $A = (7.53 \pm 0.13) \times 10^{-3}$, with a goodness-of-fit per degree of freedom of $\chi^2/\text{dof} = 3.77$. The larger deviation of the M-shell measurement from the fit function is still compatible with statistical fluctuations. The free fit is chosen as the final result to allow for the possibility of temperature dependence in the Fano factor and any other unaccounted effects.

TABLE I. Peak resolutions from Run 2 for the baseline noise and three ^{71}Ge -activation peaks.

Peak	Energy (keV _{ee})	Resolution (eV _{ee})
Baseline	0.0	9.25 ± 0.11
M Shell	0.16	18.6 ± 4.2
L Shell	1.30	31 ± 2
K Shell	10.37	101 ± 1

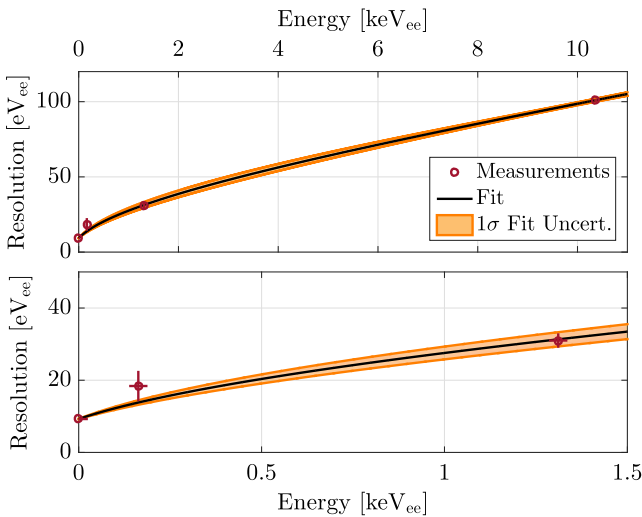


FIG. 18. Width of four points in the Run 2 energy spectrum (red points), the best-fit curve (black), and 68% uncertainty band (orange). The bottom panel is an enlargement of the top panel below 1.5 keV_{ee}.

B. Run 2 trigger efficiency and threshold

During WIMP-search data taking, the traces from all detectors were recorded when the experiment triggered. For calibration data, only the detectors in the same tower as the triggering detector were recorded. Recall that the experiment triggered if the analog sum of any detector's phonon traces exceeded a user-set hardware threshold. In anticipation of better low-frequency noise rejection, the hardware trigger threshold was lowered for Run 2 compared to Run 1, and again within Run 2, between Period 1 and Period 2.

For Run 2, the analysis thresholds were defined as the energy at which the detector's trigger efficiency reached 50%. The trigger efficiency for a given detector D was determined using events that triggered one of the other detectors and may or may not have deposited energy in detector D . The efficiency at a given energy E was then given by the fraction out of all events with energy E in detector D that also generated a trigger in detector D . The ^{252}Cf calibration data set, which has more recorded events than the WIMP-search data set, was used to measure trigger efficiency, with strict cuts applied to remove nonparticle interactions that also caused triggers, i.e., due to noise or detector cross-talk.

Two cuts were used to remove low-frequency noise, which triggered the detector at a high rate and could bias the trigger efficiency calculation, from the calibration data. The first was a pulse-shape cut based on the $\Delta\chi^2_{\text{LF}}$ parameter defined in Sec. III C 2, and the second was based on the cryocooler timing discussed in Sec. III C 1. The $\Delta\chi^2_{\text{LF}}$ -based cut was independent of energy and tighter than the energy-independent portions of the WIMP-search-data specific cut of Sec. III C 2. A tighter cut was used to be

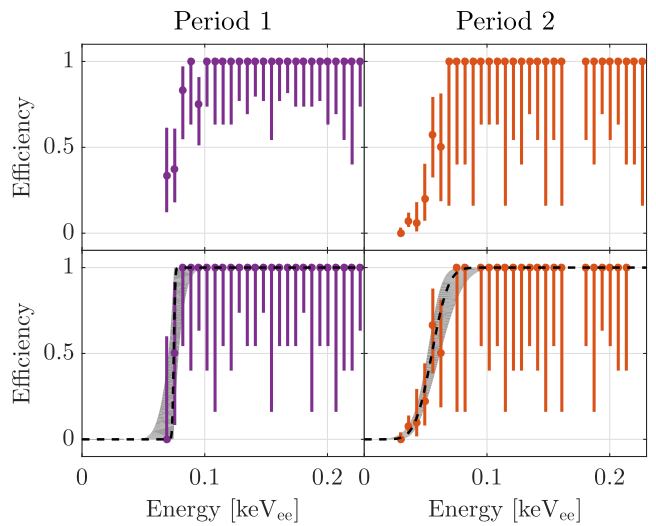


FIG. 19. Binned trigger efficiency without (top) and with (bottom) a cut on cryocooler timing for Run 2 Periods 1 (left) and 2 (right). Using the cryocooler information noticeably improved the Period 1 measurement while marginally improving that for Period 2. The best-fit error function (black dashed curve) and its 68% uncertainty (gray shaded) are given in the bottom row for each period.

particularly cautious against using low-frequency noise in the calculation.

The binned trigger efficiency shown in the top row of Fig. 19 is the result of using the pulse-shape-based cut alone. The highest-energy nonunity bin in Period 1 is at 95 eV_{ee}. The highest-energy events that failed to trigger the detector in Period 1 were found to coincide with the high-rate periods of the cryocooler cycle; i.e., they were contaminated with low-frequency noise and therefore are not representative of true physical events. The second row in Fig. 19 shows the binned efficiency after applying the second cut against low-frequency noise, removing the high-rate periods of the cryocooler cycle. After this second cut, the highest-energy nonunity bin in Period 1 shifts to 82 eV_{ee}.

The absence of accelerometer data in Period 2 was discovered very soon after the end of the run. Given the utility of the cryocooler timing information in determining the Period 1 trigger efficiency, a dedicated Period 2 ^{252}Cf calibration was performed with the accelerometers properly configured. The binned Period 2 trigger efficiency is shown in the right panels of Fig. 19. The difference between applying the cryocooler timing or not is marginal, retrospectively unsurprising considering the better state of the cryocooler following the repair. The highest-energy nonunity bin for the final Period 2 calculation is at 62 eV_{ee}. As a verification, the computation was repeated, for both Period 1 and Period 2, using the lower-rate WIMP-search data, and consistent results were found.

The final 50% trigger efficiency points come from fitting the resulting events' energy to an error function by maximizing an unbinned log-likelihood function which

contains a rising error function for events that do trigger the CDMSlite detector and a falling error function for those that do not. Both functions are needed as the event energies themselves are used in the fit as opposed to a binned passage fraction. The log-likelihood function is

$$\ln \mathcal{L}(\mu, \sigma) = \sum_i^{N_+} \ln f_+(E_i; \mu, \sigma) + \sum_j^{N_-} \ln f_-(E_j; \mu, \sigma), \quad (14)$$

where N_{\pm} is the number of events passing/failing the trigger condition on the CDMSlite detector and

$$f_{\pm}(E_i; \mu, \sigma) = 0.5 \left[1 \pm \text{erf} \left(\frac{E_i - \mu}{\sqrt{2}\sigma} \right) \right], \quad (15)$$

where E_i is the total phonon energy of the given event and μ and σ are the 50% point and width of the error function, respectively. A Markov chain Monte Carlo simulation was used to scan the parameter space, with a log-normal prior on σ and flat prior on μ . The prior on σ was required as the turn on is very sharp in Period 1; the log-normal prior inputs knowledge of the detector's resolution to prevent fits with an unphysical turn on. The best-fit values give thresholds of $\mu = 75^{+4}_{-5}$ and 56^{+6}_{-4} eV_{ee} for the two periods with the corresponding curves and 68% uncertainty bands shown in the bottom panel of Fig. 19.

V. EFFECTS OF BIAS VOLTAGE VARIATION

The bias applied at the detector, and therefore the NTL amplification, varied with time because of the presence of parasitic resistances in the biasing-electronics chain. This variation affected the calibration of the ER and NR energy scales, which thus required empirical correction. Additionally, the observed energy scale of Run 2 calls the assumed bias potential of Run 1 into question, though the effect on the Run 1 result is found to be small compared to other uncertainties.

A. Total phonon energy scale

The measured scale for total phonon energy E_t is determined by calibrating the TES-readout units of amperes to keV_t using calibration data taken at the standard iZIP operating bias of 4 V. In Run 1, the location of the strong ⁷¹Ge K -shell activation peak at ~ 120 keV_t, close to the expected 124 keV_t, was taken as confirmation of this procedure, and E_t was then converted to $E_{r,ee}$ using Eq. (7) with an assumed -69 V bias.

However, this procedure did not match the expectation in Run 2, both for the final -70 V data as well as initial -60 V data taken during Run 2 commissioning. The peak appears at 135 and 154 keV_t for -60 and -70 V, respectively, both of which are $\sim 23\%$ higher than expected. This is now understood as the effect of a bias-dependent ionization extraction and collection efficiency. For these detectors, the collection efficiency is $< 100\%$ at 4 V, while

being at or above 100% at CDMSlite biases ($> 100\%$ is possible because of impact ionization [44]). These effects were not well understood at the time of Run 1. For Run 2, the calibration from E_t to $E_{r,ee}$ was thus performed empirically by scaling the energy such that the K -shell peak appeared at the expected 10.37 keV_{ee} (see Sec. V C).

The Run 2 study thus implies a problem with the interpretation of the data from the first run, as the observed NTL amplification in the second run was noticeably higher than in the first run though the nominal bias voltages were similar at -69 and -70 V. In Run 2, the high-voltage power-supply current was measured, verifying that the bias at the detector was close to the nominal 70 V. However, such a measurement was not done during Run 1, and postrun inspections of the high-voltage biasing board indicated deterioration of a sealant epoxy, originally applied to the biasing electronics to prevent humidity-related effects. Thus, it is possible that a significant leakage current across the bias resistor, which would have reduced the effective bias voltage at the detector, went undetected. Assuming that the ionization collection efficiency was the same for both runs, and using the energy calibration from Run 2, the Run 1 peak location indicated that the effective bias potential was approximately -55 V. This $\sim 20\%$ difference in NTL gain affected the final Run 1 results and is considered in the next section.

B. Effect of gain variation on nuclear-recoil energy scale in Run 1

The NTL-amplification gain was measured by tracking variations of the total phonon energy of the 10.37 keV activation line with time. The line's intensity decreased exponentially with an 11.43 d half-life [23] and increased whenever a ²⁵²Cf calibration was performed. This activation line is shown as a function of time during Run 1 in Fig. 20. The measured energy of this line shows variations up to 15%. In the Run 1 analysis, this variation was corrected for by an empirical piecewise polynomial fit to the K -shell peak. The different colors in Fig. 20 indicate the parts of the run that were fit with independent polynomials.

These variations of the total phonon energy scale, from the inferred 20% correction due to calibration and the observed time dependence, necessarily affected the nuclear-recoil energy scale, and hence the threshold and final limit. As described Sec. I, the effect of varying the threshold can be non-negligible. Thus, it is imperative to understand what a 10%–20% variation in total phonon energy implies for the nuclear-recoil energy scale.

The effect of reducing the potential difference, compared to the assumed 69 V, is estimated by considering the relation between the reconstructed energies $E_{r,nr}$ and $E_{r,ee}$ as given by Eq. (8). At any given $E_{r,ee}$, $E_{r,nr}$ is calculated, assuming the standard Lindhard yield model, for both the original 69 V and at the reduced potential difference. A 10%–20% reduction in the potential difference

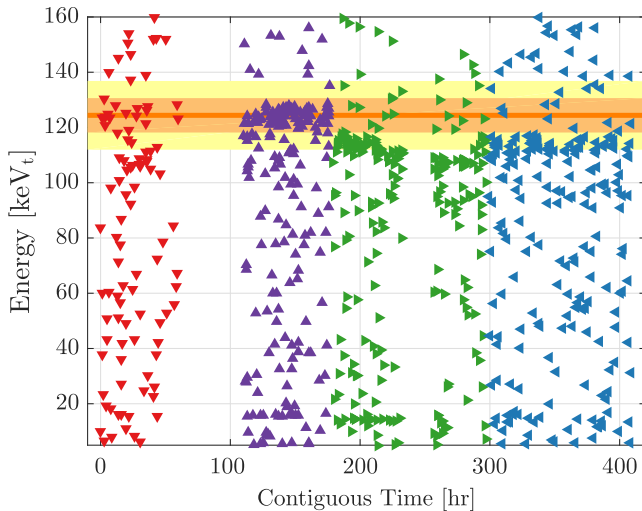


FIG. 20. Phonon energy as a function of run time for Run 1. The overdensity around 120 keV_t is from the 10.37 keV K -shell electron-capture products. Gaps exist because of unstable conditions. The different colors/orientations of the triangles indicate the four time periods which were fit to independent polynomials in the gain-correcting piecewise fit. The horizontal line indicates the peak's expected location (under the assumptions made for the Run 1 analysis; see main text) with departures of 5% and 10% indicated by the bands. The measured energy of the line shows up to 15% variation over the course of the run.

has minimal effect on the nuclear-recoil energy scale. The maximum fractional change at the Run 1 threshold for gain drops of 10%, 15%, and 20% are $|\delta E_{\text{r},\text{nr}}|/E_{\text{r},\text{nr}}(170 \text{ eV}_{\text{ee}}, -69 \text{ V}) = 1.7\%, 2.7\%$ and 3.8% , respectively. In terms of absolute energy scale, these correspond to a variation of $< 5 \text{ eV}_{\text{nr}}$ at threshold. Reevaluating the Run 1 result assuming a -55 V bias, as indicated in the previous section, leads to a 2.7% drop in threshold, which in turn leads to an improvement of the sensitivity for lower-mass WIMPs of up to 12%, while the sensitivity to higher-mass WIMPs decreases by about 2%. This is less than the uncertainty due to the ionization yield model as shown in Fig. 3. In conclusion, a 10%–20% drop in gain, even if unaccounted for, does not significantly impact the interpretation of the Run 1 result in terms of the sensitivity to low-mass WIMPs.

C. Gain correction in Run 2

Laboratory testing after Run 1 revealed that the bias variations were likely due to humidity on the high-voltage biasing board, leading to varying parasitic resistances $R_p \sim \mathcal{O}(10 \text{ M}\Omega)$, parallel to a biasing resistance of $R_b \sim 400 \text{ M}\Omega$. A new circuit was designed with a biasing resistance of $R_b \sim 200 \text{ M}\Omega$. The board was specially treated in an ultrasonic bath, baked, and layered with HumiSeal® (HumiSeal, Westwood, MA), reducing the effects of parasitic resistances under humid conditions to $R_p \gtrsim \mathcal{O}(1 \text{ G}\Omega)$. See Appendix A of Ref. [38] for details of the biasing board.

For Run 2, the DAQ was configured to record the bias V_b and current I_b of the high-voltage power supply for each event. Changes in the current are indicative of changes in total resistance encountered by the power supply, i.e., some combination of R_b and R_p . The recorded current was then used to correct the energy scale on an event-by-event basis as

$$E_{\text{t}}^{\text{Corr}} = E_{\text{t}} \cdot \frac{1 + eV_b/\epsilon_{\gamma}}{1 + e(V_b - I_b R)/\epsilon_{\gamma}}, \quad (16)$$

where R is the encountered resistance. A fit of E_{t} versus I_b demonstrated that $R \approx R_b$; i.e., R_p is much greater than R_b , is parallel to the detector, and is downstream of R_b . Based on this fit and a measured bias current $I_b \lesssim 10 \text{ nA}$, a $\lesssim 2\%$ correction was applied.

In addition to the position dependence mentioned in Sec. II C, which gave a correction of 0%–3%, two other sources of gain variation were identified in Run 2: the cryostat base temperature and discrete shifts that were possibly caused by changes in the noise environment. The base temperature of the experiment ranged from 47 – 52 mK and was recorded by the DAQ for each event. These temperature differences caused a $\lesssim 3\%$ variation in the energy scale that was corrected using the recorded temperature. After correcting for leakage current and base temperature, the mean value of the ^{71}Ge K -shell peak was consistent in time throughout Period 1. However, there were two distinct populations in Period 2, one lower than Period 1 by 2.87% and the other higher than Period 1 by 0.81%. The origin of these shifts was not identified. They were corrected for by scaling the means of the activation peak distributions to match that of Period 1. A comparison of the initial to final keV_t energy scale over the duration of Run 2 is given in Fig. 21. The mean of the final distribution was then used to scale to the $E_{\text{r},\text{ee}}$ energy scale.

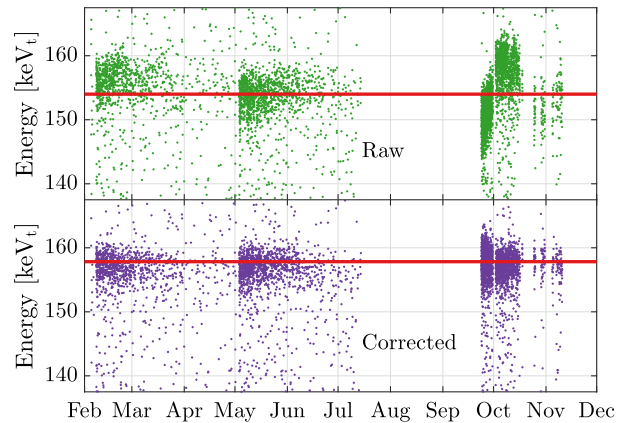


FIG. 21. K -shell activation peak (cluster at 150 – 160 keV_t) in Run 2 as a function of time without (top) and with (bottom) corrections for gain variations. ^{252}Cf calibrations occurred in February, May, and September/October. The horizontal lines indicate the means of the two peak distributions.

VI. CDMSLITE BACKGROUNDS

CDMSlite is an ER background-limited search because it cannot discriminate between ER and NR events. However, efforts have been made to understand and reduce the overall background rate in order to extend sensitivity to smaller WIMP scattering cross sections. Operating a SuperCDMS iZIP detector in CDMSlite mode required grounding one side of the detector, which created an asymmetric electric-field geometry. This geometry was studied in simulation to understand how it affects ER background modeling. Motivated by this understanding of the electric field, a fiducial volume was defined in Run 2 to remove areas of the detector where the electric-field configuration led to reduced signal amplification and therefore a higher background rate at low energies. Defining a fiducial volume thus significantly reduced the background rate in Run 2.

A. Run 2 radial fiducial-volume cut motivation

The two primary reasons to apply a radial fiducial-volume cut are to remove events of which the energy reconstruction is inaccurate and to remove low-energy background events (e.g., ^{222}Rn daughters on the detector surfaces and surrounding material). Such a cut was not applied in the Run 1 analysis as the small data set did not allow the impact of the cut to be properly assessed. With the larger Run 2 exposure, however, a radial fiducial-volume study became possible. The Run 2 cut was particularly motivated by further study of the CDMSlite electric-field configuration and an unexpected instrumental background population.

1. Improved understanding of electric-field effects

A copper detector housing enclosed the crystal radially with a small gap between the detector edge and the grounded housing. Such an arrangement, coupled with the asymmetric biasing configuration, led to an inhomogeneous electric field. The field geometry was modeled by finite-element simulation using COSMOL MULTIPHYSICS® software (COMSOL, Inc., Burlington, MA). The simulation only included a single detector, and thus any effects from the biased detectors above and below the CDMSlite detector were not included. The resulting electric field showed in which parts of the detector freed charges were attracted to the sidewall, and the grounded housing outside, rather than the grounded flat face. These regions experienced reduced NTL phonon emission and therefore a reduced reconstructed energy compared to events of the same initial-energy deposition in the bulk of the detector.

To further quantify the position-dependent effective bias voltage due to field inhomogeneities, a Monte Carlo simulation was performed of the detector crystal considering the calculated field map. In this simulation, electron-hole pairs were placed at various points throughout the detector volume and allowed to propagate according to the

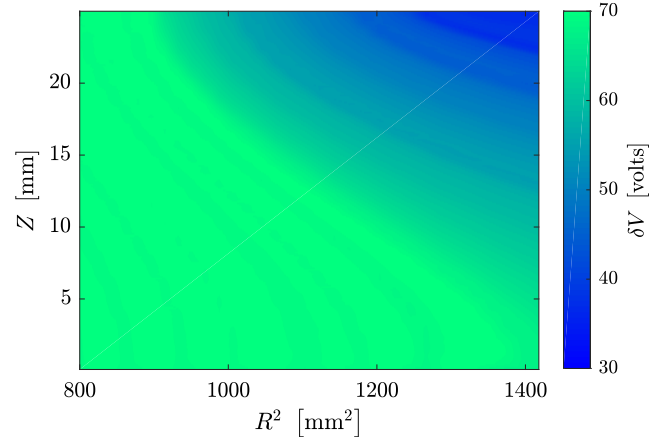


FIG. 22. Difference in electric potential between the final locations of electrons and holes (color map), after propagating through the crystal, as a function of their initial position in the detector. A single vertical slice of the detector, perpendicular to the circular top and bottom faces (see Fig. 2) and along an arbitrary radius (R coordinate, with 0 at the center of the detector) is shown. To uniformly cover the crystal, the squared radius is sampled, and thus R^2 is plotted. The top of the crystal (along the Z coordinate) is at 70 V, and the bottom is at 0 V. The copper housing (not shown at high R^2) surrounding the detector is also at 0 V, and a small gap exists between it and the sidewall. This causes the total potential difference experienced by drifting charges to be < 70 V in regions where field lines terminate on the sidewall. Radii with $R^2 < 800 \text{ mm}^2$ experience the full 70 V potential difference and are not shown.

electric-field map.⁵ The difference in electric potential at the final positions of the charge carriers was recorded for each pair, allowing for the construction of a potential difference map $\delta V = f(x, y, z)$. A slice of this map is given in Fig. 22 and shows the region of reduced potential near the sidewall and the biased face.

The reduced NTL phonon emission at the edge of the detector has the effect of smearing the energy response to lower energies. Of particular interest is the effect on the ^{71}Ge K-shell peak, which has visible smearing in the nonfiducialized Run 2 data as shown in Fig. 23. To estimate this smearing, sample events were drawn from a flat spectrum to model the Compton background, plus a Gaussian peak distribution, with the rate, mean, and width of the distributions chosen to match the observed spectrum. Next, a position was uniformly selected in the crystal, and the corresponding potential drop from $\delta V = f(x, y, z)$ was used. For every sample from the initial spectrum, E_i^{init} , the energy E_i^{final} expected to be measured for an interaction at the respective position in the detector was calculated as

⁵The electrons travel along the direction of the field at high bias voltages. Thus, oblique propagation and internally scattering mechanisms were disabled in order to increase the efficiency of the simulation.

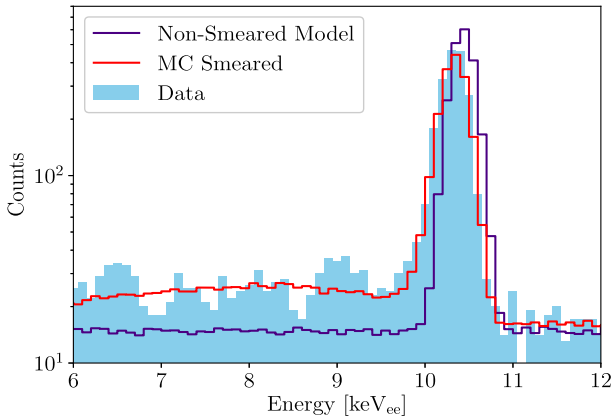


FIG. 23. ^{71}Ge K -shell peak in the Run 2 data, with no fiducial-volume cut, compared to the results of the electric-field study. The study simulates peak events on top of a flat Compton background before applying a smearing function. The smeared low-energy tail observed in the data is replicated in the simulation.

$$E_i^{\text{final}} = E_i^{\text{init}} \times \frac{1 + e\delta V_i/\epsilon_\gamma}{1 + eV_b/\epsilon_\gamma}, \quad (17)$$

where V_b is the applied 70 V bias. The result of this smearing is also shown in Fig. 23. The asymmetric peak observed in the data, as expected from the reduced NTL gain, is matched by the smeared simulation. The smearing also partially explains the rise in counts below the peak.

The Run 1 analysis did not apply a cut to remove events from this region of the detector; nor did it account for this smearing in the assumed WIMP-recoil spectrum used for deriving the published upper limit. The effect on the Run 1 result was studied postpublication by considering the fractional change of the cumulative above-threshold WIMP spectrum due to smearing the spectrum. The smear decreased the expected above-threshold WIMP spectrum by $\lesssim 5\%$ for WIMP masses above 3 GeV/c^2 . The change to the published results would thus be well within the uncertainty associated with the ionization yield model shown in Fig. 3.

The simulation and study performed here are sufficient to identify the electric field as the source of the observed spectral smearing. They are insufficient, however, for use in the analysis of the measured data, as they cannot inform how to remove the low-gain events. Regions at high radius are clearly seen to be most affected. However, a map of the true physical location as derived from accessible position-dependent analysis parameters is not known *a priori*, requiring an in-depth simulation of the phonon propagation and signal formation in the detector. Such a simulation is under development by SuperCDMS [45]. The underlying physics is understood and implemented in these simulations, but work is still needed to match simulated pulses to data. Thus, these simulations could not be used for the studies presented here.

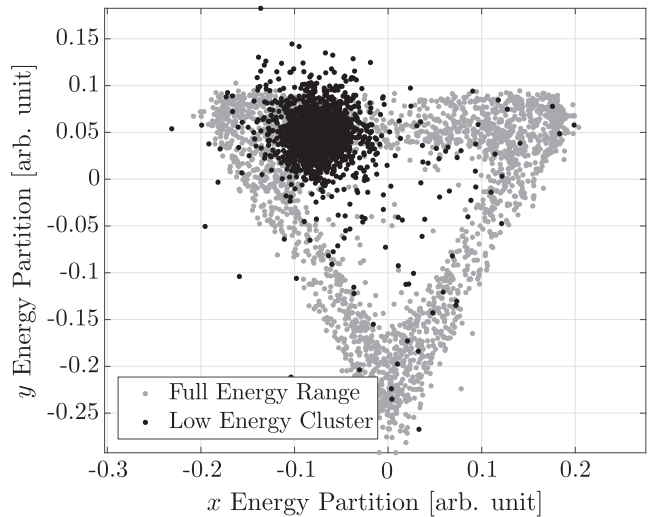


FIG. 24. Position of Run 2 events using the energy partition coordinates. Events in the full energy range are gray, while those between 100 and 200 eV_{ee} are highlighted in black. The population at low energy is clearly clustered in position.

2. Localized instrumental background

In Period 2 of Run 2, an instrumental background appeared at 100–200 eV_{ee} . These events are identifiable as background as they are localized in time, only occurring during Period 2, and position. This position localization can be seen in an x - y -plane representation shown in Fig. 24, where the positions X_{OF} and Y_{OF} are computed by the partition of energy between the three inner channels as

$$X_{\text{OF}} = \frac{\cos(30^\circ)D_{\text{OF}} + \cos(150^\circ)B_{\text{OF}} + \cos(270^\circ)C_{\text{OF}}}{B_{\text{OF}} + C_{\text{OF}} + D_{\text{OF}}} \quad (18)$$

$$Y_{\text{OF}} = \frac{\sin(30^\circ)D_{\text{OF}} + \sin(150^\circ)B_{\text{OF}} + \sin(270^\circ)C_{\text{OF}}}{B_{\text{OF}} + C_{\text{OF}} + D_{\text{OF}}} \quad (19)$$

where B_{OF} , C_{OF} , and D_{OF} are the OF fit amplitudes for the three inner channels and the angles correspond to their relative locations (cf. Fig. 2); events at the corners of the triangle correspond to events that are predominately underneath a single channel's sensors. The events in the energy range of the low-energy cluster are highlighted and localized near the top left corner, implying that they are localized in a single channel. The exact source of these events is unknown, but their localization in time and position identifies them as an instrumental background that can be removed, as shown in the next section.⁶

⁶Similar instrumental backgrounds have been observed during early CDMSlite testing of other detectors.

B. Run 2 radial fiducial-volume cut implementation

A fiducial-volume algorithm was developed based on the position information from the 2T fit (defined in Sec. II C). The channel nearest the event has the highest fast-amplitude contribution (see Fig. 7) and the earliest pulse onset. These features are used to define a new radial parameter with improved position resolution, which is used to exclude events at high radius [39]. The parameter was derived in several steps:

- (1) Correct for time variations: correct the energy-carrying slow-template amplitude for each channel in the same manner as described in Sec. V C. Derive the corrected fast amplitude N_f^{Corr} (where N stands for the channel labels $A-D$) by applying these same correction factors to the fitted fast-template amplitude.
- (2) Correct for spatial variations: for channel N , calculate a relative calibration coefficient $\xi_{N,2T}$ by normalizing the average of the slow-template amplitude over all good pulses in the energy region of interest to the respective average of channel A . This ensures that the energy scale is the same in all sensors.
- (3) Determine a weight factor for each channel. This is done in three steps:
 - (a) Determine peakiness: for channel N , the peakiness P_N is given by the corrected fast amplitude N_f^{Corr} scaled by the relative calibration factor $\xi_{N,2T}$ of that channel normalized by the total energy of the event $E_{\text{r,ee}}$ as defined in Sec. V C:

$$P_N = \xi_{N,2T} \cdot N_f^{\text{Corr}} / E_{\text{r,ee}}. \quad (20)$$

P_N will be high for channels close to the interaction point.

- (b) Determine the delay: for channel N , the delay Δ_N is given by the difference of the 2T-fit delay parameters for that channel, $\delta_{N,2T}$, and for the total phonon pulse, $\delta_{\text{tot},2T}$:

$$\Delta_N = \delta_{N,2T} - \delta_{\text{tot},2T}. \quad (21)$$

Δ_N will be low for channels close to the interaction point.

- (c) The weight factor W_N for channel N is now defined as the difference between the delay and the peakiness:

$$W_N = \Delta_N - P_N. \quad (22)$$

W_N will be low for channels close to the interaction point.

- (4) Construct a preliminary radial parameter $R_{0,2T}$ as the difference between the weight of the outer channel and that of the inner channel that is closest to the interaction point:

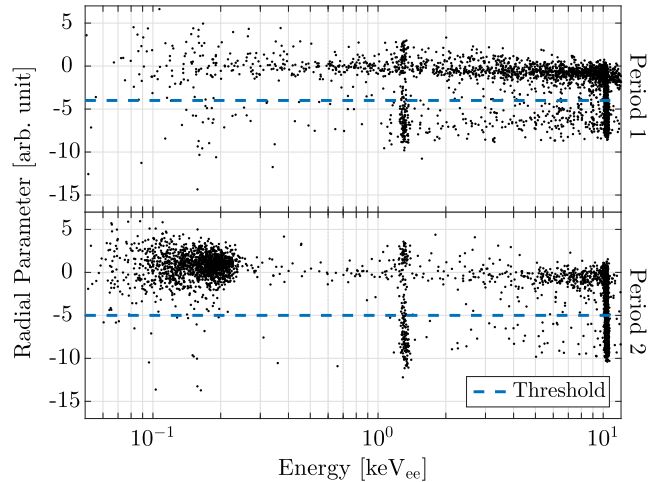


FIG. 25. 2T-fit-based radial parameter as a function of energy for Run 2 Period 1 (top) and Period 2 (bottom). The vertical clusters are the ^{71}Ge -activation lines, and the horizontal band at high radius contains reduced-amplification events. The radial cut thresholds are indicated by the blue dashed line, effectively removing events at high radius, including the low-energy cluster seen in Period 2.

$$R_{0,2T} = \min(W_B, W_C, W_D) - W_A. \quad (23)$$

$R_{0,2T}$ is low for events in the center of the detector and high for events near the edge.

- (5) Construct x - and y -positions X_{2T} and Y_{2T} in the same manner as the numerators of Eqs. (18) and (19) using the weights derived here instead of the OF-fitted amplitudes.
- (6) Derive the final radial parameter R_{2T} by correcting for a systematic dependence on angular position, reflecting the threefold symmetry of the sensor layout, that is observed in the X_{2T} versus Y_{2T} plane.

Figure 25 shows the final R_{2T} as a function of reconstructed energy. A higher density of events is seen at higher radius, and the ^{71}Ge -activation peaks are visible as vertically oriented populations at 1.30 and 10.37 keV_{ee}. The low-energy instrumental background in Period 2 is also visible, localized at high radial parameter. Note that events from within the cluster were not used in defining the radial parameter. It is obvious that R_{2T} is a nonlinear function of the true radius; the event density in the activation lines (particularly the L -shell peak) shows a clear decrease with increasing radius and then rises when the edge events begin to contribute. The cut threshold in the radial parameter, given by the dashed horizontal lines in Fig. 25, was chosen empirically on the falling edge of the radial distribution of the inner events of the L -shell peak, maximizing the efficiency while removing the low-energy cluster along with essentially the entire edge-event distribution. The radial distributions of the two periods differ somewhat, leading to slightly different choices of cut threshold values between the periods.

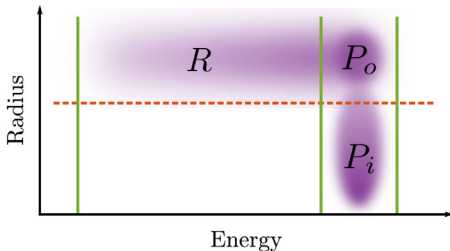


FIG. 26. Diagram showing the morphology of the expected event distribution in the radial-parameter versus reconstructed-energy plane from a monoenergetic homogeneously distributed source. The distribution is split (vertical solid lines) into nonpeak events R , with reduced NTL amplification, and peak events P . The latter group is further separated into inner peak events P_i , that pass the cut threshold (horizontal dotted line), and outer peak events P_o , that do not. In practice, the ^{71}Ge -activation peaks were considered and can be separated from background because of the known half-life of the isotope.

The signal efficiency of the radial cut was determined using the known 11.43 day half-life [23] of the ^{71}Ge produced *in situ* during neutron calibrations, together with a pulse-simulation technique. The expected distribution of events from a monoenergetic and uniformly distributed source in the plane of radial parameter versus reconstructed energy is sketched out in Fig. 26. The population is divided into two groups: events with reduced NTL amplification due to field variation (R) and those with full amplification that appear in the peak (P). The peak population is further split into two subgroups: inner events that pass the radial cut (P_i) and outer events that do not (P_o). The signal efficiency \mathcal{E} of the radial cut is defined by the probability that an individual event of the population passes the cut and appears at the expected energy:

$$\mathcal{E} = \frac{P_i}{R + P} = \frac{P}{R + P} \cdot \frac{P_i}{P}. \quad (24)$$

The second step separately calculates the fraction of events that have full NTL amplification, $\mathcal{E}_1 = P/(R + P)$, and the fraction of events with full amplification that pass the radial cut, $\mathcal{E}_2 = P_i/P$. These two factors are determined separately, taking into account the presence of background events that are not associated with the ^{71}Ge decay.

To compute \mathcal{E}_1 , the plane spanned by the radial and energy parameters was separated into several two-dimensional bins with notably different concentrations of K -shell capture events. The event distribution as a function of time was then fit, within each of these bins, with the sum of a constant and an exponential with an 11.43 day half-life, to separate the background from the ^{71}Ge contribution. The known ratio of K - to L -capture events, together with the assumption that the energy reduction is based on the electric-field geometry and thus proportional to the recoil energy, was used to identify the distribution of K -capture events at energies below the L -capture line. Following the

steps outlined in this paragraph gives $\mathcal{E}_1 = 86 \pm 0.9\%$, where the uncertainty is statistical, and due to the finite number of events in each radius versus energy bin. For the chosen cut position, more than 90% of the events with reduced energy are removed. This calculation also provides \mathcal{E}_2 for the K -shell activation line as $\mathcal{E}_2 = 54.5 \pm 1.9\%$ and $49.8 \pm 1.7\%$ for Periods 1 and 2, respectively. The total signal efficiency at the K -shell peak is then $\mathcal{E} = 47.3 \pm 1.7\%$ for Period 1 and $43.2 \pm 1.6\%$ for Period 2.

To determine \mathcal{E}_2 at lower energies, a pulse-simulation method was implemented. All events from the L -peak were converted to quasi-noise-free pulses by combining the fast and slow templates from the 2T fit according to their respective fit amplitudes for each of the phonon channels. The K -peak would have provided considerably more events; however, because of saturation of the 2T-fit-fast-template amplitude in the outer channel above $\sim 2 \text{ keV}_{ee}$ ⁷, these were not a good representation of the low-energy events, and thus could not be used for this study. The noise-free pulses were then scaled to each of 13 different energies between 0.04 and 1.30 keV_{ee} before measured noise traces were added. The full L -shell population was scaled to each energy, as opposed to using subpopulations for each, because of the limited number of peak events. In each case, the measured noise was taken from the same time period as the original pulse. At each scaled energy, the same combination of the L -peak event and noise event was used. By using the measured 2T-fit fast/slow amplitude ratio for the simulated pulses, the radial distribution of the L -shell peak events was simulated at each energy.

The cut efficiency was then measured by applying the chosen radial cut to the distribution of artificial events at each energy, accounting for the radial distribution of signal and background as measured in and around the L -peak. At lower scaled energies, some events which were close to, and on one side of, the cut threshold in the original L -shell sample moved to the other side because of the added noise. However, threshold crossing occurred in both directions; therefore, the overall cut efficiency stayed almost constant down to the lowest energies tested, as shown in Fig. 27. The uncertainty on \mathcal{E}_2 contains statistical uncertainty due to the limited number of L -shell peak events (same for each energy simulated), statistical uncertainty due to the number of simulated events that passed the cut (different for each energy simulated), and a systematic uncertainty on the estimate of nonpeak background events simulated (same for each energy simulated).

C. Effect of the delay parameter in the radial efficiency calculation

As discussed in the previous section, the radial parameter was constructed from a combination of 2T-fit amplitude

⁷The onset of this saturation was used to determine the upper energy threshold for events used in the final WIMP results.

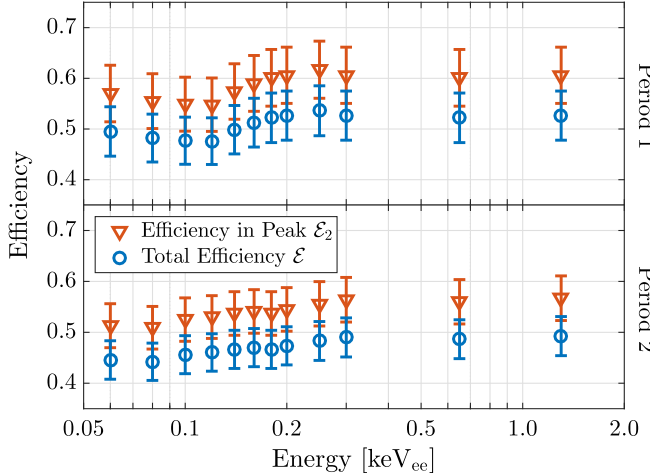


FIG. 27. Radial fiducial-volume cut efficiency below $2 \text{ keV}_{\text{ee}}$ for Period 1 (top) and Period 2 (bottom). The efficiency at full NTL amplification \mathcal{E}_2 (orange triangles) as well as the total efficiency \mathcal{E} (blue circles) are shown along with their respective uncertainties. The error bars on \mathcal{E}_2 encompass statistical uncertainty due to the available number of L -shell peak events used as simulation inputs (same for each energy simulated), statistical uncertainty due to the number of simulated events passing the cut (different for each energy simulated), and a systematic uncertainty due to the estimate of nonpeak background events simulated (same for each energy simulated). The error bars on \mathcal{E} additionally contain a small statistical uncertainty from the computation of the efficiency to have full NTL amplification (same for each energy simulated).

differences and the relative delay of the outer and primary inner phonon channels. The pulse simulation used to compute the radial cut efficiency, described in the previous section and implemented for the original publication of the Run 2 data [12], only considered the relative amplitude of the input L -shell events without including the relative delay. In order to confirm that this omission did not introduce any significant systematic uncertainty, a new version of the pulse simulation that included this relative delay of the input pulses was tested. The largest change between the original implementation and the improved version of the pulse simulation is seen at $60 \text{ eV}_{\text{ee}}$, just above threshold in Period 2, where the central value of the

efficiency drops by about 6%. However, all changes are well within the statistical uncertainties (typically $\pm 10\%-15\%$). Given the lack of statistical significance, this modification was not propagated into any final results.

D. Background rates and energy dependence

The effectiveness of the Run 2 radial fiducial-volume cut in reducing the background rate can be seen by comparing the resulting spectrum to that of Run 1 (Fig. 5). These spectra show the energy of events that scatter only in the CDMSlite detector, called “single scatters.” Single-scatter events are of interest as WIMPs are expected to scatter extremely rarely, whereas photons and electrons often scatter multiple times in the detector array giving “multiple scatters.” Multiple-scatter events were removed from the analysis of both data sets to reduce the background rate, with a loss of $< 2\%$ in signal efficiency for both analyses.

In both spectra, the germanium activation lines are seen to be on top of a continuous background, primarily from Compton scattering γ 's. The average rate between the various activation peaks and analysis thresholds are given in Table II for both analyses. The Run 2 rate above the K -shell peak is reduced by a factor of 6 from the Run 1 rate by the fiducial-volume cut. The Run 2 rates are also significantly reduced at lower energies compared to those of Run 1, though some energy dependence is seen.

Previous measurements of the Compton background at higher energies indicated a flat rate of ~ 1.5 counts ($\text{keV}_{\text{ee}} \text{ kg d}$) $^{-1}$ [46]. As shown in Table II, this rate was confirmed above the K -shell activation line in Run 1. Additionally, the measurements show that, below this peak, the overall background rate increased toward lower energy in both analyses. The increase in rate going from above to below the K -shell peak can be explained by the decay of cosmogenic isotopes within the detector and, for the Run 1 spectrum, ^{71}Ge events with reduced NTL amplification (see Sec. VIA 1).

The Run 1 spectrum shows a further increase in rate below the L -shell peak. A statistical test to compare the single- and multiple-scatter spectra was performed to understand this energy region. The Run 1 multiple-scatter spectrum is shown together with the single-scatter spectrum

TABLE II. Average single-scatter event rate for energy regions between the activation lines in Run 1, the full Run 2 exposure, and the two periods within Run 2. All errors contain $\pm \sqrt{N}$ counting uncertainties, and the Run 2 values additionally include uncertainty from the analysis efficiency (negligible in Run 1). For Run 2 Period 1, the first energy bin cuts off at that period's threshold of $75 \text{ eV}_{\text{ee}}$. See the text for discussion on the various rates.

Range (keV_{ee})	Run 1 Rate ($\text{keV}_{\text{ee}} \text{ kg d}$) $^{-1}$	Run 2 Rate ($\text{keV}_{\text{ee}} \text{ kg d}$) $^{-1}$		
		Full	Period 1	Period 2
0.056–0.14	below threshold	16 ± 8	2.5 ± 1.3	26 ± 10
0.17–1.1	5.5 ± 1.0	1.1 ± 0.2	1.2 ± 0.2	0.86 ± 0.43
1.5–7.5	2.7 ± 0.3	0.97 ± 0.07	0.95 ± 0.08	1.1 ± 0.2
12–22	1.5 ± 0.2	0.25 ± 0.03	0.26 ± 0.03	0.20 ± 0.06

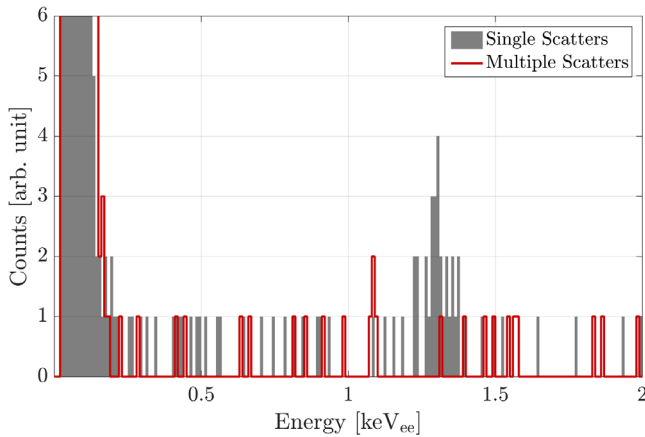


FIG. 28. Run 1 low-energy spectrum showing both single- (gray shaded) and multiple-scatter (red line) events. Below the L -shell peak, the shape of the multiple-scatter spectrum is statistically compatible with the shape of the single-scatter spectrum.

below 2 keV_{ee} in Fig. 28. These two spectra were compared by performing a Kolmogorov-Smirnov (KS) test using the energies for events between the L -shell peak and threshold. The test accepts the hypothesis that these two spectra are drawn from the same underlying probability distribution functions, giving a p-value of 79.24% that is considerably above the standard 5% hypothesis acceptance limit for a KS test. This shows that the shape of the single-scatter spectrum is consistent with that of the WIMP-free multiple-scatter spectrum, and thus the increase at low energy cannot be taken as an indication of a WIMP signal. This is further supported by the fact that the single-scatter rates above and below the L -shell peak in the Run 2 spectrum are statistically compatible with each other.

The Run 2 spectrum shows an increase in rate going from above to below the M -shell peak. Comparing the two periods of Run 2 in this energy range gives insight into this excess. For all energy regions above the M -shell peak, the two periods' rates are statistically consistent. Below the M -shell peak, however, the rate in Period 2 is dramatically higher compared to Period 1. This indicates that the increase in rate is likely due to background events leaking past the selection cuts. Such leakage is generally expected at lower energies, and leakage of the localized instrumental background in Period 2 (Sec. VIA 2) can explain the difference between the periods.

Further studies of the rate require a detailed knowledge of the shape of all expected background distributions. The spectral shape of Compton recoils at very low energies is actively being studied. A recent simulation study of the effects of atomic shell structure using GEANT4 [47] has shown that the Compton spectrum should not be expected to be flat [48]. Tritium and other low-energy background sources (e.g., ²¹⁰Pb daughters) will additionally modify the expected spectral shape and are still being studied with simulations. Future analyses will attempt to take this information into account.

VII. NEW RUN 2 DARK MATTER RESULTS

This section presents new results based on the Run 2 analysis, including the effect of varying astrophysical parameters on the spin-independent limit, as well as limits on spin-dependent interactions.

A. Effects of varying astrophysical parameters

The astrophysical description of the WIMP halo described in Sec. I enters the differential WIMP-rate expression through the halo-model factor $\mathcal{I}_{\text{halo}}$, which depends on the velocities of the WIMPs v , the velocity of the Earth with respect to the halo v_E , and the local dark matter mass density ρ_0 . As defined in Eq. (2), this factor is an integral over the assumed velocity distribution of the halo with respect to the Earth $f(v, v_E)$.

The limits computed for both Runs 1 and 2 assume the standard halo model (SHM) for the dark matter spatial and velocity distributions. The SHM assumes an isotropic, isothermal, and nonrotating sphere of dark matter in which the Galaxy is embedded. The velocity distribution associated with this model is a Maxwellian distribution boosted to the lab frame of the Earth as

$$f(v, v_E) \propto \exp(-|v + v_E|^2/2\sigma_v^2), \quad (25)$$

where the proportionality constant has already been subsumed into Eq. (2) and the velocity dispersion is $\sigma_v^2 = v_0^2/2$, where v_0 is the large-radius asymptotic Galactic circular velocity. It is typically assumed that this asymptotic value has been reached at the Sun's position [10], giving $v_0 = \Theta_0 \equiv |\Theta_0|$. Θ_0 is the Galactic local standard of rest (LSR), corresponding to the average circular orbital velocity at the Sun's distance from the Galactic center.⁸ The Earth's velocity is decomposed as $v_E = \Theta_0 + v_\odot + v_\oplus$, where the other velocities are v_\odot , the solar peculiar velocity with respect to neighboring stars, and v_\oplus , the Earth's orbital velocity around the Sun. The Earth's orbital velocity is assumed to average to zero over a year. Integrating this distribution over the range of velocities described in Sec. I gives Eq. (3). Note that the maximum velocity used in the integration, which is related to the Galactic escape velocity v_{esc} , truncates the theoretical distribution which would otherwise extend to infinite velocities.

The direct-detection experimental community has been using a uniform set of measurements for each of these parameters in its analyses: $\rho_0 = 0.3 \text{ GeV c}^{-2} \text{ cm}^{-3}$ [1], $\Theta_0 = 220 \pm 20 \text{ km s}^{-1}$ in the direction of Galactic rotation [49], $v_{\text{esc}} = 544^{+64}_{-46} \text{ km s}^{-1}$ [50], and $v_\odot = (11.0 \pm 1.2, 12.24 \pm 2.1, 7.25 \pm 1.1) \text{ km s}^{-1}$, where the

⁸The LSR is of interest to astronomers regardless of whether this assumption is true, and thus the Θ_0 notation, common in the astrophysical literature, is used for the LSR and its equality to v_0 only taken when specifically referring to the SHM.

first component is the radial velocity toward the Galactic center, the second component is in the direction of Galactic rotation, and the third component is the vertical velocity (out of the Galactic plane) [51]. It is well known that the uncertainties in these values, in particular Θ_0 and v_{esc} , can have significant effects on computed WIMP exclusion limits [52], and thus astrophysical uncertainties are also expected on the CDMSlite Run 2 spin-independent result. Although the local dark matter density is also uncertain [53], all experiments are equally affected by its value, so the effect of its uncertainty on the Run 2 limit is not considered further.

For this astrophysical-parameter discussion, the Run 2 analysis uncertainties are not considered. Upper limits are computed using the central efficiency curve in Fig. 4 and the standard Lindhard model with $k = 0.157$: a set of parameters labeled “best fit.”⁹ All other assumptions about the rate discussed in Secs. I and II B are left unchanged, and the optimum interval method [31] is again used to compute limits.

The SHM value of v_{esc} comes from the median and 90% confidence region of the 2007 RAVE survey study [50]. The RAVE survey collaboration released an updated study of the escape velocity in 2014 [54] in which they found a slightly lower median and reduced uncertainty span of $v_{\text{esc}} = 533^{+54}_{-41} \text{ km s}^{-1}$. Varying the escape velocity changes the lower edge of the WIMP-mass range, as a higher maximum halo velocity allows lower-mass WIMPs to deposit energy above threshold. The effect on the Run 2 limit of varying the escape velocity while keeping all other SHM parameters constant can be seen in Fig. 29. The difference between the 2007 and 2014 RAVE medians is negligible at all but the lowest WIMP masses.

Recent measurements of the magnitude of the LSR Θ_0 are numerous [55] and include different approaches in measurement technique, galactic modeling, and prior assumptions. The range that the collection of results spans, $196\text{--}270 \text{ km s}^{-1}$, is broader than any individual uncertainty, which indicates possible systematic uncertainties between the measurements and models. The effect of varying Θ_0 on the Run 2 limit, keeping all other halo parameters at their standard values, can be seen in Fig. 30. Varying Θ_0 , and therefore the most probable velocity in the distribution v_0 , changes where the most sensitive part of the curve lies in addition to changing the lowest accessible WIMP mass. This uncertainty has a large effect at the lowest WIMP masses, shifting the limit on σ_N^{SI} by up to an order of magnitude in either direction.

The effect of jointly varying Θ_0 and v_{esc} is considered by computing the limit 1000 times, each time selecting a different set of velocity parameters from their respective

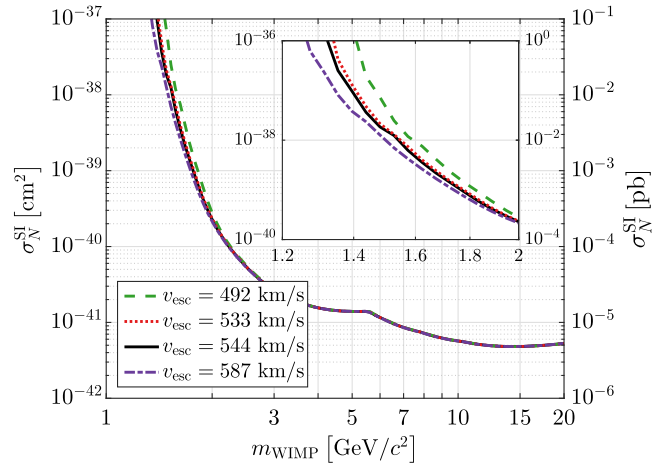


FIG. 29. Effect on the Run 2 best-fit limit from varying the Galactic escape velocity v_{esc} in the Maxwellian halo model while keeping all other parameters constant. Curves shown are the median values of the 2007 and 2014 RAVE survey results at 492 km s^{-1} (black solid) and 533 km s^{-1} (red dotted), respectively, as well as the 90% confidence bounds of the 2014 result at 492 km s^{-1} (green dashed) and 587 km s^{-1} (purple dot-dashed). The inset shows an enlargement below WIMP masses of $2 \text{ GeV}/c^2$. Varying v_{esc} changes the lowest WIMP mass that can produce recoils above threshold, while the impact on the limit at higher masses is negligible.

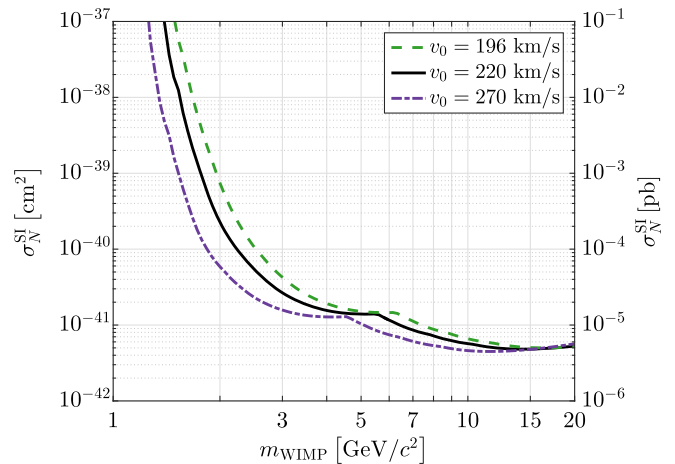


FIG. 30. Effect on the Run 2 best-fit limit from varying the most probable WIMP velocity Θ_0 in the Maxwellian halo model while keeping all other parameters constant. Curves shown are for the SHM value of 220 km s^{-1} (black solid) and the upper and lower bounds of the measured values at 270 km s^{-1} (green dashed) and 196 km s^{-1} (purple dot-dashed). Varying Θ_0 changes where the most sensitive part of the curve lies in addition to slight changes in the lowest accessible WIMP mass. The effect is largest for the lowest WIMP masses, vertically shifting the limit by up to an order of magnitude in either direction.

⁹Calling this the “best fit” is a slight misnomer as no actual fitting was performed to obtain the values.

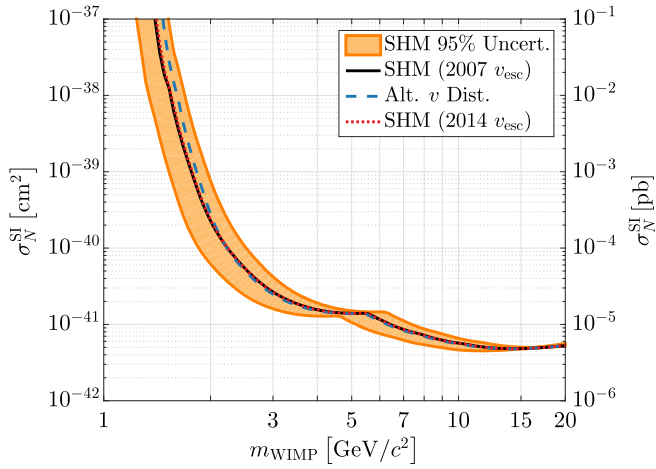


FIG. 31. The 95% (orange) uncertainty band on the best-fit Run 2 spin-independent limit (black solid) due to the uncertainties in the most probable WIMP velocity (v_0) and the Galactic escape velocity (v_{esc}) used in the SHM. The 2014 RAVE survey v_{esc} distribution is sampled, and thus the best-fit curve substituting the 2014 median value into the SHM is given for consistency (red dotted). The black and red-dotted curves are the same as in Fig. 29, where an enlargement at low WIMP mass is given. The best-fit limit computed using the alternative velocity distribution of Eq. (26) is also presented (blue dashed).

distributions. For Θ_0 , a conservative flat distribution between the bounding measurements, $196\text{--}270 \text{ km s}^{-1}$, is sampled. For v_{esc} , the probability distribution of v_{esc} from the 2014 RAVE study (distribution graciously provided by the study authors) is directly sampled. The 95% central interval from the 1000 limit curves is shown in

Fig. 31 around the SHM-value curve. The size of the uncertainty band is comparable to the uncertainty band on the analysis uncertainties given in Fig. 3. Note also that Ref. [54] demonstrates an anticorrelation between Θ_0 and v_{esc} , meaning that the computed uncertainty band, which samples the velocity values independently, is an overestimate of the combined uncertainty.

Finally, an alternative WIMP velocity distribution is also considered in Fig. 31. The model is that of Mao *et al.* [56], which gives, in the rest frame of the dark matter,

$$f(v) \propto e^{-v/v_a}(v_{\text{esc}}^2 - v^2)^p, \quad (26)$$

where v_a and p are parameters of the model. Fits to a Milky-Way-like simulation with baryons give $p = 2.7$ and $v_a/v_{\text{esc}} = 0.6875$ [57]. The distribution is boosted to the lab frame via the usual $v \rightarrow v + \Theta_0 + v_\odot + v_\oplus$, where the SHM values for these astrophysical velocities are used. This model naturally tends to $v = 0$ at the escape velocity, which explains the reduced sensitivity at the lightest WIMP masses seen in the limit curve.

B. Spin-dependent limits on WIMPs

While the SuperCDMS technology is most sensitive to spin-independent WIMP-nucleon scattering, the presence of a neutron-odd isotope, ^{73}Ge ($N = 41$) with an abundance in natural Ge of 7.73%, yields competitive limits for spin-dependent scattering at low WIMP masses [58].

The differential elastic-scattering cross section for a fermionic WIMP with respect to the momentum transferred to the nucleus q is given by

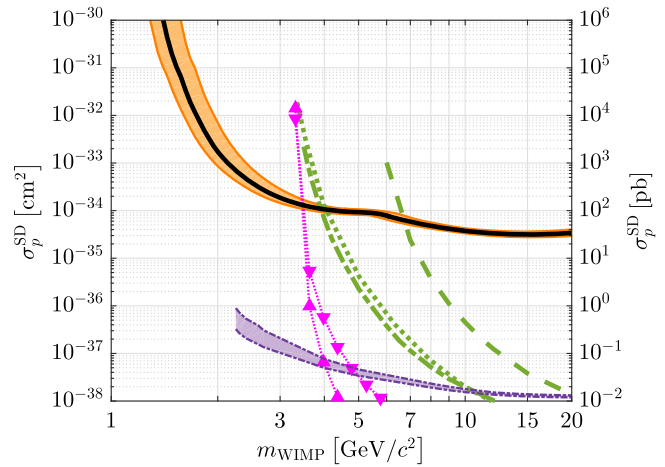
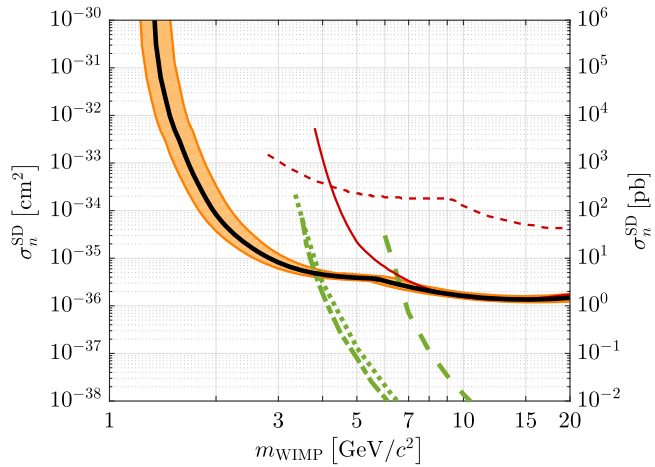


FIG. 32. Upper limits on the spin-dependent free neutron σ_n^{SD} (left) and free proton σ_p^{SD} (right) WIMP scattering cross sections in the proton- and neutron-only models, respectively. For both, the median (90% C.L.) (thick black solid curve) upper limit from CDMSlite Run 2 is compared to other selected direct-detection limits from PANDAX-II (thick-green dotted curve) [61], LUX (thick-green dot-dashed curve) [62], XENON100 (thick-green dashed curve) [63], PICO-60 (magenta upward triangles) [64], PICO-2L (magenta downward triangles) [65], PICASSO (purple dot-dashed band) [66], CDEX-0 (thin-red dashed curve) [67,68], and CDEX-1 (thin-red solid curve) [68]. The orange band surrounding the Run 2 result is the 95% uncertainty interval on the upper limit. The Run 2 limits are the most sensitive for $m_{\text{WIMP}} \lesssim 4$ and $\lesssim 2 \text{ GeV}/c^2$ for the neutron- and proton-only models, respectively.

$$\frac{d\sigma^{\text{SD}}}{dq^2} = \frac{8G_F^2}{(2J+1)v^2} S_T(q), \quad (27)$$

where G_F is Fermi's constant, J is the total nuclear spin of the target nucleus, and $S_T(q)$ is the momentum-transfer-dependent spin-structure function. $S_T(q)$ can be parameterized into isoscalar S_{00} , isovector S_{11} , and interference S_{01} terms as

$$S_T(q) = a_0^2 S_{00}(q) + a_1^2 S_{11}(q) + a_0 a_1 S_{01}(q), \quad (28)$$

where the isoscalar and isovector coupling coefficients are related to the proton and neutron couplings as $a_0 = a_p + a_n$ and $a_1 = a_p - a_n$. Explicit forms of $S_T(q)$ are obtained from detailed nuclear models for specific isotopes.

The scattering cross section is typically written in a form similar to the spin-independent case as

$$\frac{d\sigma^{\text{SD}}}{dq^2} = \frac{8G_F^2}{(2J+1)v^2} S_T(0) F_{\text{SD}}^2(q), \quad (29)$$

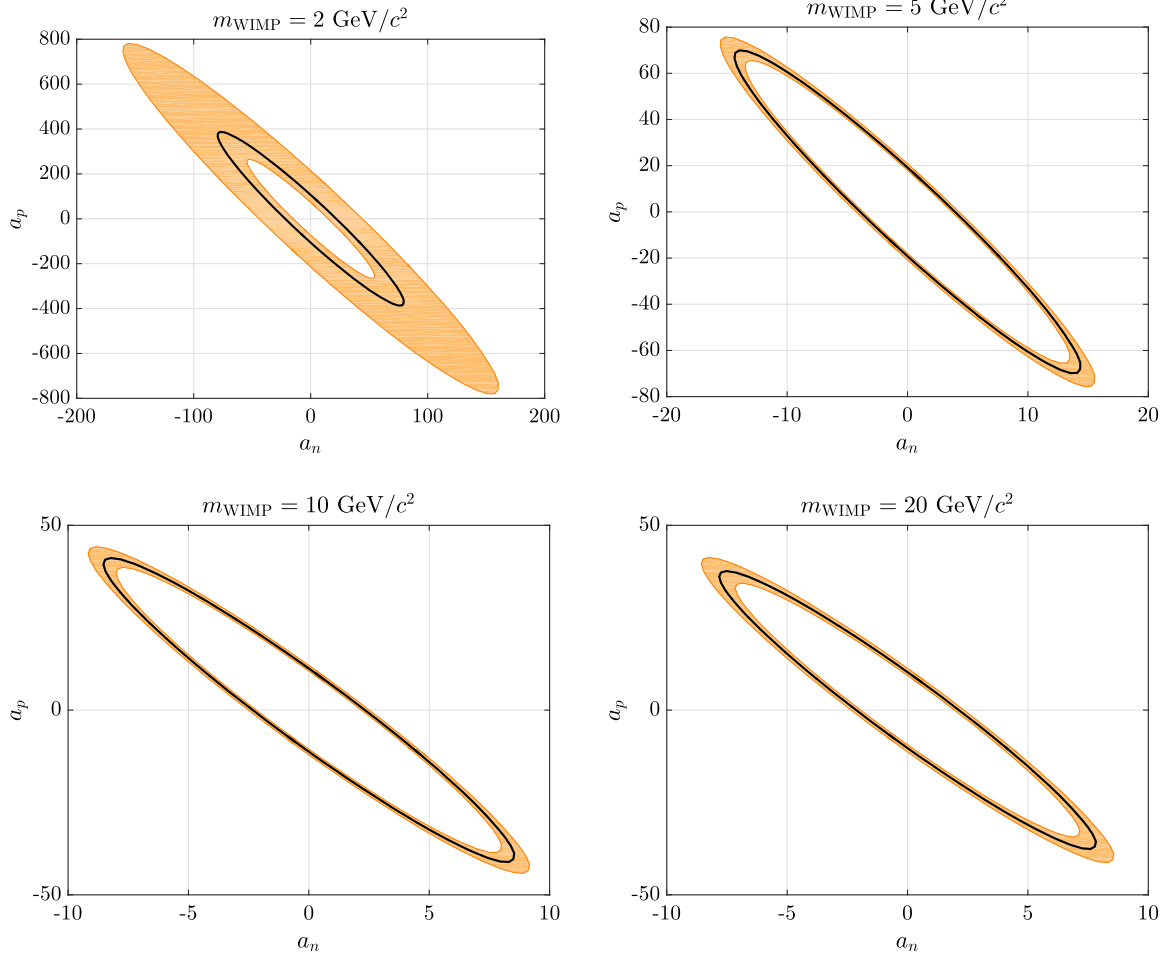
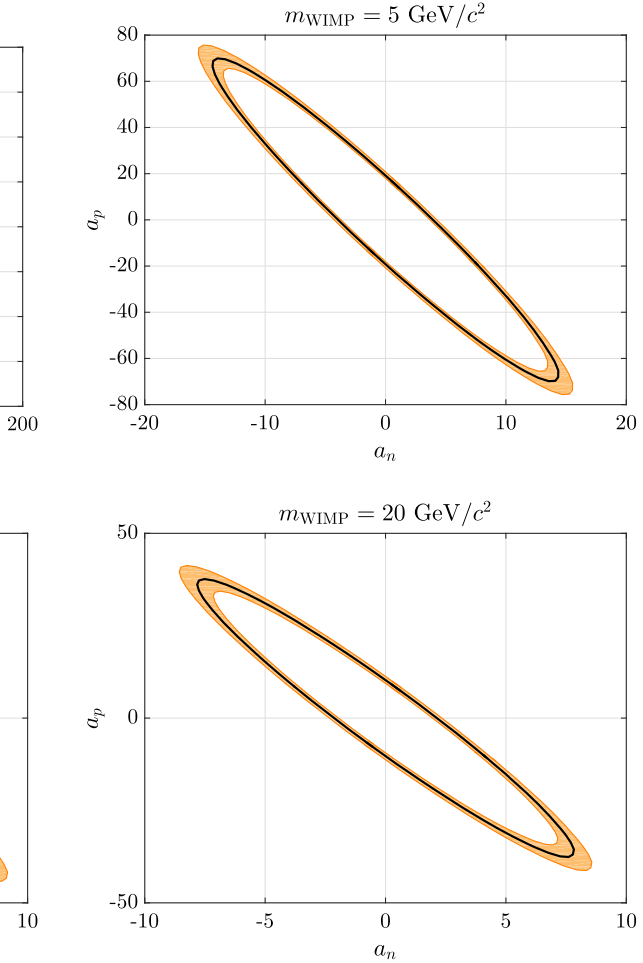


FIG. 33. Median (90% C.L.) upper limit and associated 95% uncertainty (thick black solid curve and orange bands) on the WIMP-nucleon coupling coefficients a_p and a_n from CDMSlite Run 2 for WIMP masses of 2 (top left), 5 (top right), 10 (bottom left), and 20 (bottom right) GeV/c^2 . Areas outside the ellipses are excluded for each WIMP mass.

where $F_{\text{SD}}^2(q) \equiv S_T(q)/S_T(0)$ is the form factor of Eq. (1), which is normalized to unity at zero momentum transfer ($q \rightarrow 0$). In that limit, the structure function is

$$S_T(0) = \frac{(2J+1)(J+1)}{4\pi J} |(a_0 + a'_1)\langle S_p \rangle + (a_0 - a'_1)\langle S_n \rangle|^2, \quad (30)$$

where $a'_1 = a_1(1 + \delta a_1(0))$ includes contributions from two-body current scattering as given by Klos *et al.* in Ref. [59]. In two-body current scattering, the WIMP effectively interacts with two nucleons in the nucleus, via the $\delta a_1(0)$ term. The expectation values of the proton and neutron groups within the nucleus $\langle S_p \rangle$ and $\langle S_n \rangle$ are computed from nuclear theory and usually $\langle S_p \rangle \gg \langle S_n \rangle$ for proton-odd nuclei and vice versa for neutron-odd nuclei. Note that, although the spin coupling to the even-nucleon species is weak, the inclusion of two-body currents allows for WIMP-proton-neutron effective interactions. Thus, the



odd-nucleon-species coupling dominates the scattering calculations for any coupling type.

The standard cross section σ_0^{SD} from Eq. (1) is defined as the total cross section in the $q \rightarrow 0$ limit,

$$\sigma_0^{\text{SD}} = \frac{32}{2J+1} G_F^2 \mu_T^2 S_T(0). \quad (31)$$

The differential cross section can then be written as

$$\frac{d\sigma^{\text{SD}}}{dq^2} = \frac{1}{4\mu_T^2 v^2} \sigma_0^{\text{SD}} F_{\text{SD}}^2(q), \quad (32)$$

where $\mu_T = m_\chi m_T / (m_\chi + m_T)$ is the reduced mass of the WIMP-nucleus system. Results are presented in the “proton-only” model where $a_p = 1$ and $a_n = 0$, implying $a_0 = a_1 = 1$, and the “neutron-only” model where $a_p = 0$ and $a_n = 1$, implying $a_0 = -a_1 = 1$. Results are also normalized to the scattering of a WIMP and a free proton/neutron as

$$\sigma_0^{\text{SD}} = \frac{4\pi}{3} \frac{1}{(2J+1)} \left(\frac{\mu_T}{\mu_{p/n}} \right)^2 S_T^{p/n}(0) \sigma_{p/n}^{\text{SD}}, \quad (33)$$

where $\sigma_{p/n}^{\text{SD}}$ is the free proton/neutron standard cross section, $\mu_{p/n}$ is the proton-/neutron-WIMP reduced mass, and $S_T^{p/n}(0)$ is $S_T(0)$ evaluated in the proton-/neutron-only models.

Limits set on $\sigma_{p/n}^{\text{SD}}$ using the Run 2 data and analysis are presented in Fig. 32. The limits were computed using the same framework as the spin-independent limits that is described in Sec. II B, including using the optimum interval method [31] and sampling the analysis uncertainties. The median and 95% uncertainty band from the resulting set of limits are shown in the figure for each model. The low threshold of CDMSlite gives world-leading limits for WIMP masses $\lesssim 4$ and $\lesssim 2 \text{ GeV}/c^2$ for the neutron-only and proton-only models, respectively. Limits were also computed using the older spin-structure model of Ref. [60], which does not include two-body currents. In the neutron-only case, only a mild improvement of 8% is seen using the newer Klos *et al.* model. However, using the newer model improves the proton-only limit by a factor of ~ 7 , a direct consequence of the WIMP-proton-neutron two-body current increasing the proton-only structure function.

Limits are also placed jointly on the coupling coefficients a_p and a_n for four different WIMP masses. Results in this plane were computed by converting the coefficients to polar coordinates, $a_p = a \sin \theta$ and $a_n = a \cos \theta$, and observing that for a given θ , $S_T(q) \propto a^2$. The proton- and neutron-only models are recovered for $\theta = \pi/2, 0$, respectively. Values of θ were scanned, and an upper limit was placed on a for each angle. Appendix A discusses different methods for computing these limits and includes

justification for the chosen approach. Limits in the a_p versus a_n plane are given in Fig. 33 for m_{WIMP} of 2, 5, 10, and $20 \text{ GeV}/c^2$. Regions outside of the ellipses are excluded. The limits were again computed by sampling the analysis uncertainties with the median and 95% intervals for each WIMP mass given in the figure.

VIII. SUMMARY AND OUTLOOK

This paper described in detail the CDMSlite technique for extending dark matter direct detection searches to WIMP masses of $\sim 1.5 \text{ GeV}/c^2$ by achieving analysis thresholds as low as $56 \text{ eV}_{\text{ee}}$. New analysis techniques were presented and applied to the first two CDMSlite data sets taken with the SuperCDMS Soudan experiment, yielding new limits on spin-dependent interactions and a better understanding of the effects of astrophysical uncertainties on the limits.

There is one more Soudan CDMSlite data set, taken with a different detector, to be analyzed. Previous studies have indicated that this different detector is less sensitive to low-frequency noise, and preliminary studies with the new CDMSlite data show a 50% trigger efficiency point as low as $50 \text{ eV}_{\text{ee}}$. This data set will be used to develop improved CDMSlite analysis techniques, including a salting scheme to mitigate analyzer bias, further understanding of the electric-field influence on fiducial volume, and low-energy background modeling to test background subtraction techniques.

The SuperCDMS Collaboration is also designing a new experiment, SuperCDMS SNOLAB, where the CDMSlite technique will be used in detectors designed specifically for high-voltage operation. Planned improvements with such detectors include [69] two-sided biasing, which diminishes the reduced bias region of the detector; increasing the surface area coverage of the phonon sensor; operating at higher applied potentials; and fabricating TESs with lower operational temperatures for the phonon read-out. With the latter two improvements, the SuperCDMS Collaboration aims at thresholds $\lesssim 10 \text{ eV}_{\text{ee}}$ that will correspondingly provide sensitivity to WIMP masses as low as $400 \text{ MeV}/c^2$ [70].

ACKNOWLEDGMENTS

The SuperCDMS Collaboration gratefully acknowledges technical assistance from the staff of the Soudan Underground Laboratory and the Minnesota Department of Natural Resources, as well as the many contributions of David Caldwell, who passed away during the writing of this article. The iZIP detectors were fabricated in the Stanford Nanofabrication Facility, which is a member of the National Nanofabrication Infrastructure Network, sponsored and supported by the NSF. Part of the research described in this article was conducted under the Ultra Sensitive Nuclear Measurements Initiative and under Contract No. DE-AC05-76RL01830 at Pacific Northwest National Laboratory, which is operated by Battelle for the

U.S. Department of Energy. Funding and support were received from the National Science Foundation, the Department of Energy, Fermilab URA Visiting Scholar Award No. 13-S-04, NSERC Canada, and MultiDark (Spanish MINECO). Fermilab is operated by the Fermi Research Alliance, LLC, under Contract No. De-AC02-07CH11359. SLAC is operated under Contract No. DEAC02-76SF00515 with the United States Department of Energy.

APPENDIX: SETTING LIMITS ON SPIN-DEPENDENT COUPLING COEFFICIENTS WITH TWO-BODY CURRENTS

A model-independent method for setting joint limits on the spin-dependent coupling constants a_p and a_n was derived by Tovey *et al.* in Ref. [71]. In that work, the authors derive a simple expression relating the allowed values of the coupling constants, for a given WIMP mass, as

$$\frac{\pi}{24G_F^2\mu_p^2} \geq \left[\frac{a_p}{\sqrt{\sigma_p^L}} \pm \frac{a_n}{\sqrt{\sigma_n^L}} \right]^2, \quad (\text{A1})$$

where G_F is Fermi's constant, $\sigma_{p/n}^L$ are the limits on the free-proton/-neutron cross sections for the given WIMP mass (assuming a proton-/neutron-only interaction), the small difference between the WIMP-proton μ_p and WIMP-neutron μ_n reduced masses is ignored, and the sign in the

brackets is the same as the ratio of nuclear spin-group expectation values $\langle S_n \rangle / \langle S_p \rangle$. This expression is derived from the observation that the allowed total-nucleus cross section σ_0^{SD} must be smaller than the limit set upon it by a given analysis σ_0^L . Equation (A1) is then found by using the expression for the zero-momentum spin structure function $S_T(0)$ without two-body currents, found by taking $\delta a_1(0) \rightarrow 0$ in Eq. (30).

Including the two-body current contributions to $S_T(0)$ from Klos *et al.* [59] changes this derivation and result. Starting with $\sigma_0^{\text{SD}} / \sigma_0^L \leq 1$ and using Eq. (31) for σ_0^{SD} and Eq. (30) for $S_T(0)$ gives

$$1 \geq \frac{8(J+1)G_F^2\mu_T^2}{J\pi} \left[\frac{|(a_0 + a'_1)\langle S_p \rangle|}{\sqrt{\sigma_0^L}} \pm \frac{|(a_0 - a'_1)\langle S_n \rangle|}{\sqrt{\sigma_0^L}} \right]^2, \quad (\text{A2})$$

where the sign of the \pm is determined by the sign of $(a_0 - a'_1)\langle S_n \rangle / (a_0 + a'_1)\langle S_p \rangle$. The limits on the total cross section are not factored out as they are next rewritten in terms of the limits on the free-proton/-neutron cross sections $\sigma_{p/n}^L$ in the proton-/neutron-only models, as given by Eq. (33). In the denominator of the left term, the proton-only model form is used, while the neutron-only form is used under the right term. The resulting inequality after changing coupling bases to that of the proton and neutron couplings is

$$\frac{\pi}{24G_F^2\mu_p^2} \geq \left[\frac{|2a_p + (a_p - a_n)\delta a_1(0)|}{\sqrt{\sigma_p^L}} \frac{|\langle S_p \rangle|}{|[2 + \delta a_1(0)]\langle S_p \rangle - \delta a_1(0)\langle S_n \rangle|} \right. \\ \left. \pm \frac{|2a_n - (a_p - a_n)\delta a_1(0)|}{\sqrt{\sigma_n^L}} \frac{|\langle S_n \rangle|}{|-\delta a_1(0)\langle S_p \rangle + [2 + \delta a_1(0)]\langle S_n \rangle|} \right]^2. \quad (\text{A3})$$

The simpler Eq. (A1) is recovered by taking the limit of no two-body currents ($\delta a_1(0) \rightarrow 0$).

If proton-/neutron-only limits are computed using the two-body-inclusive spin-structure function, then it is inconsistent to use the simple Eq. (A1) to compute limits on the coupling constants. This is particularly important for low-mass WIMPs as the two-body current has its largest effect for low momentum transfer.

Because of the complexity of Eq. (A3), the “polar coordinate” method for computing coupling constant upper limits was used instead for the current results. This method transforms coordinates from the Cartesian (a_p, a_n) to the polar (a, θ) as

$$a_p = a \sin \theta \quad (\text{A4})$$

$$a_n = a \cos \theta. \quad (\text{A5})$$

In these new coordinates, the momentum-dependent spin-structure function (28) is

$$S_T(q) = a^2 [(1 + \sin 2\theta)S_{00}(q) - \cos 2\theta S_{10}(q) \\ + (1 - 2 \sin \theta \cos \theta)S_{11}(q)] \quad (\text{A6})$$

$$\equiv a^2 f(q, \theta), \quad (\text{A7})$$

where q is the momentum transferred in the collision. This form of the spin-structure function enters the standard computation by multiplying both sides of Eq. (31) by the form factor $F_{\text{SD}}^2 = S_T(q)/S_T(0) = a^2 f(q, \theta)/S_T(0)$. The polar-coordinates method is equally valid with or

without the inclusion of two-body currents depending upon the functions used for the S_{ij} . The procedure described in Sec. VII B can then be followed to construct the upper limit curves; i.e., scan over the angle θ , and compute an upper limit on a^2 for each angle.

-
- [1] K. Olive *et al.*, Review of particle physics, *Chin. Phys. C* **38**, 090001 (2014).
- [2] P. A. R. Ade *et al.* (Planck Collaboration), Planck 2015 results: XIII. Cosmological parameters, *Astron. Astrophys.* **594**, A13 (2016).
- [3] G. Jungman, M. Kamionkowski, and K. Griest, Supersymmetric dark matter, *Phys. Rep.* **267**, 195 (1996).
- [4] M. W. Goodman and E. Witten, Detectability of certain dark-matter candidates, *Phys. Rev. D* **31**, 3059 (1985).
- [5] G. Aad *et al.* (ATLAS Collaboration), Search for new phenomena in final states with an energetic jet and large missing transverse momentum in pp collisions at $\sqrt{s} = 8$ TeV with the ATLAS detector, *Eur. Phys. J. C* **75**, 299 (2015).
- [6] V. Khachatryan *et al.* (CMS Collaboration), Search for dark matter, extra dimensions, and unparticles in monojet events in proton-proton collisions at $\sqrt{s} = 8$ TeV, *Eur. Phys. J. C* **75**, 235 (2015).
- [7] D. E. Kaplan, M. A. Luty, and K. M. Zurek, Asymmetric dark matter, *Phys. Rev. D* **79**, 115016 (2009).
- [8] J. Alexander *et al.*, Dark sectors 2016 workshop: community report, [arXiv:1608.08632](https://arxiv.org/abs/1608.08632).
- [9] J. Lewin and P. Smith, Review of mathematics, numerical factors, and corrections for dark matter experiments based on elastic nuclear recoil, *Astropart. Phys.* **6**, 87 (1996).
- [10] F. Donato, N. Fornengo, and S. Scopel, Effects of galactic dark halo rotation on WIMP direct detection, *Astropart. Phys.* **9**, 247 (1998).
- [11] R. Agnese *et al.* (SuperCDMS Collaboration), Search for Low-Mass Weakly Interacting Massive Particles Using Voltage-Assisted Calorimetric Ionization Detection in the SuperCDMS Experiment, *Phys. Rev. Lett.* **112**, 041302 (2014).
- [12] R. Agnese *et al.* (SuperCDMS Collaboration), New Results from the Search for Low-Mass Weakly Interacting Massive Particles with the CDMS Low Ionization Threshold Experiment, *Phys. Rev. Lett.* **116**, 071301 (2016).
- [13] D. S. Akerib *et al.* (CDMS Collaboration), Exclusion limits on the WIMP-nucleon cross section from the first run of the Cryogenic Dark Matter Search in the Soudan Underground Laboratory, *Phys. Rev. D* **72**, 052009 (2005).
- [14] R. Agnese *et al.* (SuperCDMS Collaboration), Improved WIMP-search reach of the CDMS II germanium data, *Phys. Rev. D* **92**, 072003 (2015).
- [15] R. Agnese *et al.* (SuperCDMS Collaboration), Demonstration of surface electron rejection with interleaved germanium detectors for dark matter searches, *Appl. Phys. Lett.* **103**, 164105 (2013).
- [16] D. Bauer *et al.*, The CDMS II Data Acquisition System, *Nucl. Instrum. Methods Phys. Res., Sect. A* **638**, 127 (2011).
- [17] R. Agnese *et al.* (SuperCDMS Collaboration), Search for Low-Mass Weakly Interacting Massive Particles with SuperCDMS, *Phys. Rev. Lett.* **112**, 241302 (2014).
- [18] B. Neganov and V. Trofimov, Calorimetric method measuring ionizing radiation, *Otkrytia Izobret.* **146**, 215 (1985); USSR Patent No. 1037771 (1981) (in Russian).
- [19] P. N. Luke, Voltage-assisted calorimetric ionization detector, *J. Appl. Phys.* **64**, 6858 (1988).
- [20] K. M. Sundqvist, Ph.D. thesis, University of California, Berkeley, 2012.
- [21] C. Kittel, *Solid State Phys.*, 8th ed. (Wiley, New York, 2005), p. 703.
- [22] F. E. Emery and T. A. Rabson, Average energy expended per ionized electron-hole pair in silicon and germanium as a function of temperature, *Phys. Rev.* **140**, A2089 (1965); R. Pehl, F. Goulding, D. Landis, and M. Lenzlinger, Accurate determination of the ionization energy in semiconductor detectors, *Nucl. Instrum. Methods* **59**, 45 (1968).
- [23] W. Hampel and L. P. Remsberg, Half-life of ^{71}Ge , *Phys. Rev. C* **31**, 666 (1985).
- [24] J. A. Bearden and A. F. Burr, Reevaluation of x-ray atomic energy levels, *Rev. Mod. Phys.* **39**, 125 (1967).
- [25] J. Lindhard, V. Nielsen, M. Scharff, and P. V. Thomsen, Integral equations governing radiation effects (notes on atomic collisions III), *Mat. Fys. Medd. K. Dan. Vid. Selsk.* **33** (1963); J. Lindhard, M. Scharff, and H. E. Schiott, Range concepts and heavy ion ranges (notes on atomic collisions II), *Mat. Fys. Medd. K. Dan. Vid. Selsk.* **33** (1963); J. Lindhard, V. Nielsen, and M. Scharff, Approximation method in classical scattering by screened Coulomb fields (notes on atomic collisions, I), *Mat. Fys. Medd. K. Dan. Vid. Selsk.* **36** (1968).
- [26] D. Barker and D.-M. Mei, Germanium detector response to nuclear recoils in searching for dark matter, *Astropart. Phys.* **38**, 1 (2012).
- [27] A. Soma *et al.*, Characterization and performance of germanium detectors with sub-keV sensitivities for neutrino and dark matter experiments, *Nucl. Instrum. Methods Phys. Res., Sect. A* **836**, 67 (2016).
- [28] K. W. Jones and H. W. Kranner, Energy lost to ionization by 254-eV ^{73}Ge atoms stopping in Ge, *Phys. Rev. A* **11**, 1347 (1975).
- [29] P. S. Barbeau, J. I. Collar, and O. Tench, Large-mass ultralow noise germanium detectors: performance and applications in

- neutrino and astroparticle physics, *J. Cosmol. Astropart. Phys.* **09** (2007) 009.
- [30] B. J. Scholz, A. E. Chavarria, J. I. Collar, P. Privitera, and A. E. Robinson, Measurement of the low-energy quenching factor in germanium using an $^{88}\text{Y}/\text{Be}$ photoneutron source, *Phys. Rev. D* **94**, 122003 (2016).
- [31] S. Yellin, Finding an upper limit in the presence of an unknown background, *Phys. Rev. D* **66**, 032005 (2002); Extending the optimum internal method, [arXiv:0709.2701](https://arxiv.org/abs/0709.2701).
- [32] R. H. Helm, Inelastic and elastic scattering of 187-Mev electrons from selected even-even nuclei, *Phys. Rev.* **104**, 1466 (1956).
- [33] G. Angloher *et al.* (CRESST Collaboration), Results on light dark matter particles with a low-threshold CRESST-II detector, *Eur. Phys. J. C* **76**, 25 (2016).
- [34] A. Tan *et al.* (PandaX-II Collaboration), Dark Matter Results from First 98.7 Days of Data from the PandaX-II Experiment, *Phys. Rev. Lett.* **117**, 121303 (2016).
- [35] E. Browne and J. Tuli, Nuclear data sheets for $A = 65$, *Nucl. Data Sheets* **111**, 2425 (2010).
- [36] S. A. Hertel, Ph.D. thesis, Massachusetts Institute of Technology, 2012.
- [37] S. R. Golwala, Ph.D. thesis, University of California, Berkeley, 2000.
- [38] R. Basu Thakur, Ph.D. thesis, University of Illinois, Urbana-Champaign, 2015.
- [39] M. Pepin, Ph.D. thesis, University of Minnesota, Twin Cities, 2016.
- [40] D. Abrams *et al.* (CDMS Collaboration), Exclusion limits on the WIMP-nucleon cross section from the Cryogenic Dark Matter Search, *Phys. Rev. D* **66**, 122003 (2002).
- [41] Z. I. Botev, J. F. Grotowski, and D. P. Kroese, Kernel density estimation via diffusion, *Ann. Stat.* **38**, 2916 (2010).
- [42] U. Fano, Ionization yield of radiations. II. The fluctuations of the number of ions, *Phys. Rev.* **72**, 26 (1947).
- [43] R. C. Alig, S. Bloom, and C. W. Struck, Scattering by ionization and phonon emission in semiconductors, *Phys. Rev. B* **22**, 5565 (1980).
- [44] A. Phipps, B. Sadoulet, and K. M. Sundqvist, Observation of impact ionization of shallow states in sub-Kelvin, high-purity germanium, *J. Low Temp. Phys.* **184**, 336 (2016).
- [45] S. W. Leman, Invited review article: physics and Monte Carlo techniques as relevant to cryogenic, phonon, and ionization readout of Cryogenic Dark Matter Search radiation detectors, *Rev. Sci. Instrum.* **83**, 091101 (2012).
- [46] Z. Ahmed *et al.*, Analysis of the low-energy electron-recoil spectrum of the CDMS experiment, *Phys. Rev. D* **81**, 042002 (2010).
- [47] S. Agostinelli *et al.*, Geant4a simulation toolkit, *Nucl. Instrum. Methods Phys. Res., Sect. A* **506**, 250 (2003); J. Allison *et al.*, Geant4 developments and applications, *IEEE Trans. Nucl. Sci.* **53**, 270 (2006).
- [48] D. Barker, Low energy background spectrum in CDMSlite, *Proc. Sci. ICHEP* (2016) 874 [[arXiv:1611.05792](https://arxiv.org/abs/1611.05792)].
- [49] F. J. Kerr and D. Lynden-Bell, Review of galactic constants, *Mon. Not. R. Astron. Soc.* **221**, 1023 (1986).
- [50] M. C. Smith *et al.*, The RAVE survey: Constraining the local Galactic escape speed, *Mon. Not. R. Astron. Soc.* **379**, 755 (2007).
- [51] R. Schönrich, J. Binney, and W. Dehnen, Local kinematics and the local standard of rest, *Mon. Not. R. Astron. Soc.* **403**, 1829 (2010).
- [52] C. McCabe, Astrophysical uncertainties of dark matter direct detection experiments, *Phys. Rev. D* **82**, 023530 (2010); A. M. Green, Astrophysical uncertainties on direct detection experiments, *Mod. Phys. Lett. A* **27**, 1230004 (2012); C. A. J. O’Hare, Dark matter astrophysical uncertainties and the neutrino floor, *Phys. Rev. D* **94**, 063527 (2016).
- [53] P. Salucci, F. Nesti, G. Gentile, and C. Frigerio Martins, The dark matter density at the Sun’s location, *Astron. Astrophys.* **523**, A83 (2010).
- [54] T. Piffl *et al.*, The RAVE survey: The Galactic escape speed and the mass of the Milky Way, *Astron. Astrophys.* **562**, A91 (2014).
- [55] M. J. Reid, K. M. Menten, X. W. Zheng, A. Brunthaler, L. Moscadelli, Y. Xu, B. Zhang, M. Sato, M. Honma, T. Hirota, K. Hachisuka, Y. K. Choi, G. A. Moellenbrock, and A. Bartkiewicz, Trigonometric parallaxes of massive star-forming regions. VI. Galactic structure, fundamental parameters, and noncircular motions, *Astrophys. J.* **700**, 137 (2009); J. Bovy, D. W. Hogg, and H.-W. Rix, Galactic masers and the Milky Way circular velocity, *Astrophys. J.* **704**, 1704 (2009); P. J. McMillan and J. J. Binney, The uncertainty in Galactic parameters, *Mon. Not. R. Astron. Soc.* **402**, 934 (2010); S. E. Koposov, H.-W. Rix, and D. W. Hogg, Constraining the Milky Way potential with a six-dimensional phase-space map of the GD-1 stellar stream, *Astrophys. J.* **712**, 260 (2010); V. V. Bobylev and A. T. Bajkova, Galactic parameters from masers with trigonometric parallaxes, *Mon. Not. R. Astron. Soc.* **408**, 1788 (2010); P. J. McMillan, Mass models of the Milky Way, *Mon. Not. R. Astron. Soc.* **414**, 2446 (2011); J. Bovy *et al.*, The Milky Way’s circular-velocity curve between 4 and 14 kpc from APOGEE data, *Astrophys. J.* **759**, 131 (2012); J. L. Carlin, S. R. Majewski, D. I. Casetti-Dinescu, D. R. Law, T. M. Girard, and R. J. Patterson, Kinematics and chemistry of stars along the Sagittarius trailing tidal tail and constraints on the Milky Way mass distribution, *Astrophys. J.* **744**, 25 (2012); M. Honma *et al.*, Fundamental parameters of the Milky Way galaxy based on VLBI astrometry, *Publ. Astron. Soc. Jpn.* **64**, 136 (2012); M. J. Reid *et al.*, Trigonometric parallaxes of high mass star forming regions: The structure and kinematics of the Milky Way, *Astrophys. J.* **783**, 130 (2014); V. V. Bobylev and A. T. Bajkova, Kinematic analysis of solar-neighborhood stars based on RAVE4 data, *Astron. Lett.* **42**, 90 (2016).
- [56] Y.-Y. Mao, L. E. Strigari, R. H. Wechsler, H.-Y. Wu, and O. Hahn, Halo-to-halo similarity and scatter in the velocity distribution of dark matter, *Astrophys. J.* **764**, 35 (2013); Y.-Y. Mao, L. E. Strigari, and R. H. Wechsler, Connecting direct dark matter detection experiments to cosmologically motivated halo models, *Phys. Rev. D* **89**, 063513 (2014).
- [57] A. Pillepich, M. Kuhlen, J. Guedes, and P. Madau, The distribution of dark matter in the Milky Way’s disk, *Astrophys. J.* **784**, 161 (2014).

- [58] D. S. Akerib *et al.* (CDMS Collaboration), Limits on spin-dependent WIMP-nucleon interactions from the Cryogenic Dark Matter Search, *Phys. Rev. D* **73**, 011102 (2006).
- [59] P. Klos, J. Menéndez, D. Gazit, and A. Schwenk, Large-scale nuclear structure calculations for spin-dependent WIMP scattering with chiral effective field theory currents, *Phys. Rev. D* **88**, 083516 (2013).
- [60] V. I. Dimitrov, J. Engel, and S. Pittel, Scattering of weakly interacting massive particles from ^{73}Ge , *Phys. Rev. D* **51**, R291 (1995).
- [61] C. Fu *et al.* (PandaX-II Collaboration), Spin-Dependent Weakly-Interacting-Massive-ParticleNucleon Cross Section Limits from First Data of PandaX-II Experiment, *Phys. Rev. Lett.* **118**, 071301 (2017).
- [62] D. S. Akerib *et al.* (LUX Collaboration), Results on the Spin-Dependent Scattering of Weakly Interacting Massive Particles on Nucleons from the Run 3 Data of the LUX Experiment, *Phys. Rev. Lett.* **116**, 161302 (2016).
- [63] E. Aprile *et al.* (XENON Collaboration), Low-mass dark matter search using ionization signals in XENON100, *Phys. Rev. D* **94**, 092001 (2016).
- [64] C. Amole *et al.* (PICO Collaboration), Dark Matter Search Results from the PICO-60 C_3F_8 Bubble Chamber, *Phys. Rev. Lett.* **118**, 251301 (2017).
- [65] C. Amole *et al.* (PICO Collaboration), Improved dark matter search results from PICO-2L Run 2, *Phys. Rev. D* **93**, 061101 (2016).
- [66] E. Behnke *et al.* (PICASSO Collaboration), Final results of the PICASSO dark matter search experiment, *Astropart. Phys.* **90**, 85 (2017).
- [67] S. K. Liu *et al.* (CDEX Collaboration), Limits on light WIMPs with a germanium detector at 177 eVee threshold at the China Jinping Underground Laboratory, *Phys. Rev. D* **90**, 032003 (2014).
- [68] W. Zhao *et al.* (CDEX Collaboration), Search of low-mass WIMPs with a p-type point contact germanium detector in the CDEX-1 experiment, *Phys. Rev. D* **93**, 092003 (2016).
- [69] N. Kurinsky, P. Brink, R. Partridge, B. Cabrera, and M. Pyle, SuperCDMS SNOLAB low-mass detectors: ultra-sensitive phonon calorimeters for sub-GeV dark matter search, *Proc. Sci. ICHEP* (**2016**) 1116 [[arXiv:1611.04083](#)].
- [70] R. Agnese *et al.*, Projected Sensitivity of the SuperCDMS SNOLAB experiment, *Phys. Rev. D* **95**, 082002 (2017).
- [71] D. Tovey, R. Gaitskill, P. Gondolo, Y. Ramachers, and L. Roszkowski, A new model-independent method for extracting spin-dependent cross section limits from dark matter searches, *Phys. Lett. B* **488**, 17 (2000).